φ_0-Josephson junction in twisted bilayer graphene induced by a valley-polarized state

Ying-Ming Xie,[1,*] Dmitri K. Efetov [2] and K. T. Law[1,†]

[1]*Department of Physics, Hong Kong University of Science and Technology, Clear Water Bay, 999077 Hong Kong, China*
[2]*ICFO–Institut de Ciencies Fotoniques, The Barcelona Institute of Science and Technology, Castelldefels, Barcelona 08860, Spain*

Recently, gate-defined Josephson junctions in magic angle twisted bilayer graphene (MATBG) were studied experimentally, and highly unconventional Fraunhofer patterns were observed. In this work, we show that an interaction-driven valley-polarized state connecting two superconducting regions of MATBG would give rise to a long-sought-after purely electric controlled φ_0-junction in which the two superconductors acquire a finite phase difference φ_0 in the ground state. We point out that the emergence of the φ_0-junction stems from the valley-polarized state which breaks time-reversal symmetry, and trigonal warping effects which break intravalley inversion symmetry. Importantly, a spatially nonuniform valley-polarization order parameter at the junction can explain the key features of the observed unconventional Fraunhofer patterns. Our work explores the novel transport properties of the valley-polarized state, and we suggest that gate-defined MATBG Josephson junctions could realize the first purely electric controlled φ_0-junctions.

I. INTRODUCTION

The discovery of correlated insulating states and superconducting states in magic angle twisted bilayer graphene (MATBG) [1–3] motivated intense studies of moiré materials in recent years. The rich symmetry-breaking states discovered in MATBG [4–38] enable the creation of novel quantum devices with various quantum phases on a single material platform. Recently, gate-defined Josephson junctions (JJs) were created on MATBG [39–42] when a nonsuperconducting (weak-link) region in a superconducting MATBG device was created by local gating. Interestingly, a highly unconventional Fraunhofer pattern was observed in Ref. [41] when the weak-link region was gated to near half-filling $\nu = -1/2$ filling (two holes per moiré unit cell).

The observed unconventional Fraunhofer pattern motivated us to study the Josephson effects in a gate-defined superconductor/valley-polarized state/superconductor (SC/VP/SC) in MATBG, as schematically shown in Fig. 1(a). As the unconventional Fraunhofer pattern indicates time-reversal and inversion symmetry breaking at the weak-link of the Josephson junction [41], we choose the weak link to be a partially valley-polarized state. In this case, the energy degeneracy of moiré bands of the K and $-K$ valleys is broken due to electron-electron interactions [Fig. 1(b)]. Such a valley-polarized state is one of the possible energetically

favorable states at half-filling from Hartree-Fock calculations [28–36,43], which also satisfies the symmetry requirements of the experiment. The choice of the valley-polarized state as the weak link in the Josephson junction is further motivated by the observation of the anomalous Hall effect at half-filling in a recent experiment in which the twist angle was slightly away from the magic angle [43]. This anomalous Hall effect can also be explained by the partially valley-polarized state.

In this work, we show that the current-phase relation induced by the interaction-driven valley-polarized state as the weak link of a Josephson junction is highly unconventional, and it has the form $I_s = I_c \sin(\phi - \varphi_0)$. Here, I_c is the critical current, and $\phi = \phi_L - \phi_R$ is the phase difference of the two superconductors with phases ϕ_L and ϕ_R, respectively. Such Josephson junctions with general φ_0 are called φ_0-Josephson junctions (φ_0-JJs). We further point out that the valley polarization and the trigonal warping effects are the key ingredients for realizing φ_0-JJs. Importantly, a spatially nonuniform valley-polarization order parameter at the junction can provide a plausible explanation for the unconventional Fraunhofer patterns observed in the experiment [41].

φ_0-JJs have important potential device applications, such as superconducting spintronics [44,45], Josephson qubits [46–48], and phase batteries [49]. The previously proposed realizations of φ_0-JJs involve ferromagnetic materials [50–56] or materials with spin-orbit coupling [57–70]. However, experimental realizations of φ_0-JJ were rare, and the presence of external magnetic fields was needed [49,67–69]. This work establishes a platform of realizing φ_0-JJs with the interaction-driven valley-polarized state in MATBG.

*ymxie@ust.hk
†phlaw@ust.hk

II. MODEL FOR NUMERICAL CALCULATION

First, we introduce a microscopic model that describes a MATBG Josephson junction as realized experimentally in
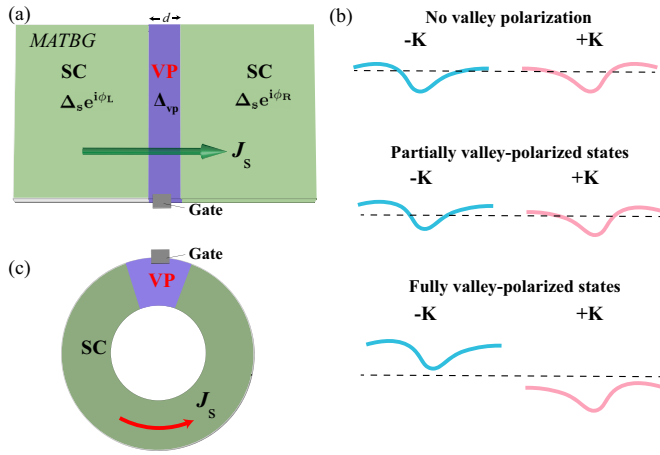
FIG. 1. (a) A schematic plot of a gate-defined MATBG Josephson junction. The left (right) side of the junction is superconducting with pairing order parameter $\Delta_s e^{i\phi_{L(R)}}$. The weak-link region has width d and a valley polarization order parameter Δ_{vp}. (b) Illustrations of the moiré bands at K and $-K$ valleys which are not valley-polarized, partially valley-polarized, and fully valley-polarized, respectively [31,43]. The black dashed lines denote the Fermi levels. (c) A schematic plot of a MATBG superconducting ring with a region gated to the valley-polarized state. The J_s (red arrow) represents a spontaneous supercurrent.

Ref. [41] and schematically shown in Fig. 1(a). The relevant moiré bands near charge neutrality of MATBG can be captured by an effective two-orbital tight-binding model on a hexagonal lattice [4,5], which can be written as

$$H_0 = \sum_{\langle ij \rangle, \xi\sigma} t_1 c_{i\xi\sigma}^\dagger c_{j\xi\sigma} + \sum_{\langle ij \rangle', \xi\sigma} t_{2\xi} c_{i\xi\sigma}^\dagger c_{j\xi\sigma} + \text{H.c.}$$
$$- \sum_{i,\xi\sigma} \mu_i c_{i\xi\sigma}^\dagger c_{i\xi\sigma}. \tag{1}$$

Here, ξ labels the two p-wave-like orbitals $p_x + i\xi p_y$ as a representation of two valleys $\tau = \pm K$, $\sigma = \uparrow / \downarrow$ denotes the spin indices, and $t_1 = 0.331$ meV and $t_{2\xi} = -0.01 + 0.097\xi i$ meV denote the first-nearest-neighbor and the fifth-nearest-neighbor hopping. Note that the imaginary part of $t_{2\xi}$ describes the warping effects. Moreover, the spatial dependent chemical potential is denoted by μ, which is chosen such that the filling factor ν satisfies $-1 < \nu < -1/2$ for the superconducting part of the junction and $\nu \approx -1/2$ at the weak-link region [41]. As shown in Refs. [4,5], H_0 captures the symmetries of the moiré bands of MATBG.

To include the effects of interactions, we introduce the superconducting order parameter on the left (L) and right (R) sides of the Josephson junction and the valley-polarization order parameter to the weak link. The resulting effective tight-binding Hamiltonian is

$$H_{\text{eff}} = H_0 + \sum_{i\in(\text{L,R}),\xi} (\Delta_s e^{i\phi_{L(R)}} c_{i\xi\uparrow}^\dagger c_{i-\xi\downarrow}^\dagger + \text{H.c.})$$
$$+ \sum_{i\in\text{WL},\xi\sigma} \Delta_{vp} c_{i\xi\sigma}^\dagger (\tau_z)_{\xi\xi'} c_{i\xi'\sigma}. \tag{2}$$

Here, the second term characterizes the pairing potential on the left and right side of the Josephson junction with phases ϕ_L and ϕ_R, respectively. To be specific, we set the spin-singlet pairing [10,71] amplitude $\Delta_s = 0.1$ meV according to the experiments [3,41], which is roughly one order smaller than the moiré bandwidth. It is important to note that other time-reversal invariant unconventional pairings have been proposed in MATBG [37,72]. For simplicity, a conventional spin-singlet pairing order parameter is assumed in the main text. The conclusions obtained here are still valid even if we assume other momentum-independent pairings which involve both the spin and valley degrees of freedom of MATBG (Appendix E). The temperature effects on the pairing can be included by setting $\Delta_s(T) = \Delta_s \tanh(1.74\sqrt{(T_c - T)/T})$ (T_c is the superconducting critical temperature) [73].

On the other hand, the third term with the Pauli matrix τ_z characterizes the valley polarization in the weak-link (WL) region with valley-polarization order parameter Δ_{vp}. The order parameter Δ_{vp} can be seen from the Hamiltonian with Coulomb interactions under the Hartree-Fock mean-field approximation (see Appendix A). More details about the tight-binding model can be found in Appendix C.

III. UNCONVENTIONAL JOSEPHSON JUNCTION INDUCED BY THE VALLEY-POLARIZED STATE

To study the properties of the gate-defined MATBG Josephson junction, we first calculate the energy dispersion as a function of the phase difference ϕ of the junction, which is described by H_{eff}. Here, we set the length of the nonsuperconducting part of the junction be $d = 10L_M/\sqrt{3}$ [41] ($L_M \approx 14$ nm is the moiré lattice constant), and set the filling ν to be close to half-filling. To match the experimental situation in which the junction resistance is much smaller than the quantized resistance h/e^2 [41], we set the weak-link regime to be partially valley-polarized [31,43] such that the weak-link section is metallic as schematically illustrated in Fig. 1(b). The case of fully valley-polarized topological state is studied in the Appendix C.

Figures 2(a) and 2(b) show a typical energy spectrum of the MATBG Josephson junction as a function of the phase difference $\phi = \phi_L - \phi_R$, obtained by diagonalizing the junction Hamiltonian H_{eff} with $\Delta_{vp}/\Delta_s = 0$ and $\Delta_{vp}/\Delta_s = 1$, respectively. As expected, there is a large number of Andreev bound states within the superconducting gap. The energy-phase relations of a few Andreev bound states with large slopes are highlighted by red solid lines in Figs. 2(a) and 2(b). It can be seen that the in-gap Andreev bound states with large slopes $\frac{\partial E}{\partial \phi}$ contributing mostly to the supercurrent exhibit a phase shift that is close to (but not equal to) π when the valley polarization $\Delta_{vp}/\Delta_s = 1$. This phase shift gives the first indication that the valley polarization has nontrivial effects on the Josephson junction.

To study the ground state of the Josephson junction, we calculate the free energy as

$$F(\phi) = -k_B T \sum_n \ln(1 + e^{-E_n(\phi)/k_B T}), \tag{3}$$

where T is the temperature, and the energy of the states $E_n(\phi)$ is obtained by diagonalizing the Hamiltonian $H_{\text{eff}}(\phi)$.
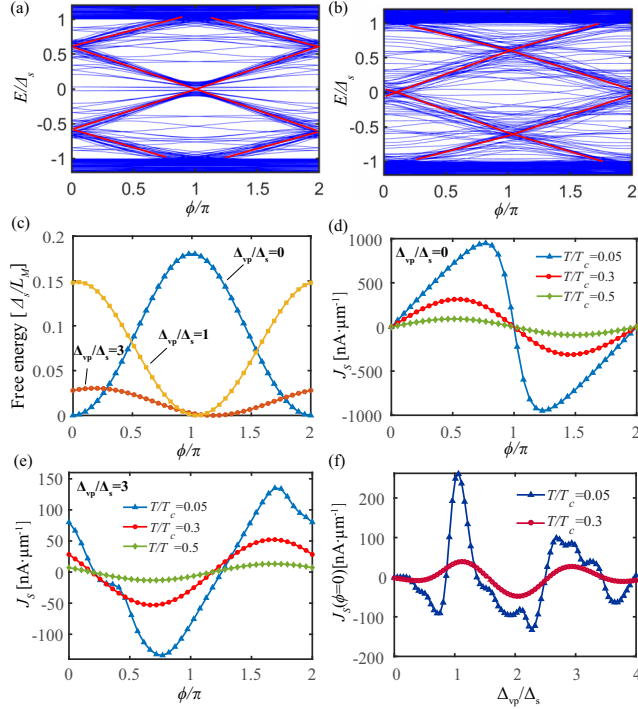
FIG. 2. (a), (b) The energy levels of a MATBG Josephson junction vs the phase difference ϕ in the cases of no valley polarization ($\Delta_{\text{vp}}/\Delta_s = 0$) and with valley polarization $\Delta_{\text{vp}}/\Delta_s = 1$, respectively, where red lines highlight the positions of Andreev bound states with large slopes. The width of the junction is $W_J = 10L_M$ and the length is $d = 10L_M/\sqrt{3}$. The filling of the weak-link region and the superconducting region are $\nu \approx -0.5$ and $\nu \approx -0.6$, respectively. (c) The landscape of the free energy $F_J(\phi)$ (in units of Δ_s/L_M) with $\Delta_{\text{vp}}/\Delta_s = 0, 1, 3$. The temperature is fixed at $T/T_c = 0.3$. (d), (e) The supercurrent density (in units of nA μm^{-1}) vs ϕ at various temperatures in the cases of $\Delta_{\text{vp}}/\Delta_s = 0$ and 3, respectively. The total supercurrent across the junction would be given by J_sW_J. (f) The anomalous supercurrent $J_s(\phi = 0)$ vs the valley polarization strength Δ_{vp} at $T/T_c = 0.05$ and 0.3.

For the sake of convenience, we define the free energy of the Josephson junction per unit width to be $F_J(\phi) = W_J^{-1}(F(\phi) - \min[F(\phi)])$, where W_J is the width of the junction. Therefore, the phase difference of the two superconductors at the ground state is determined by ϕ_0 such that $F_J(\phi_0) = 0$. In Fig. 2(c), we plot the free-energy landscapes $F_J(\phi)$ with temperature $T = 0.3T_c$ at various valley polarization strengths ($\Delta_{\text{vp}}/\Delta_s = 0, 1, 3$). As expected, without valley polarization, the junction is conventional so that the ground state appears at $\phi = 0$. Interestingly, the ground state of the Josephson junction can appear at a finite ϕ in the presence of valley polarization. For example, in the case of $\Delta_{\text{vp}}/\Delta_s = 1$, the ground state with $F_J(\phi) = 0$ appears at a phase difference close to (but not equal to) π. For a larger Δ such that $\Delta_{\text{vp}}/\Delta_s = 3$, the ground state appears at a phase further away from π.

To show the effect of valley polarization on the current-phase relation, the supercurrent density J_s (in units of nA μm^{-1}) as a function of ϕ is depicted in Fig. 2(d) for the case without valley polarization ($\Delta_{\text{vp}}/\Delta_s = 0$) and in Fig. 2(e) for the case with valley polarization ($\Delta_{\text{vp}}/\Delta_s = 3$). Here, the

supercurrent density is obtained from the free energy of the Josephson junction as $J_s = \frac{2e}{\hbar}\frac{\partial F_J(\phi)}{\partial \phi}$. Without valley polarization, the junction has a conventional current-phase relation at both the low- and high-temperature regimes [74,75]. However, in the case with finite valley polarization, the supercurrent can either exhibit a sign change or even display a generic phase shift [see Fig. 2(e)]. In particular, it can be seen that the curves with higher temperature [the red and green lines in Fig. 2(e)] follow a standard φ_0-JJ current-phase relation of $J_s = J_c \sin(\phi - \varphi_0)$. Our calculation thus clearly shows that the valley polarization can result in φ_0-JJs in MATBG.

One important consequence of a φ_0-JJ is that there is a supercurrent even at zero phase difference ($\phi = 0$), called anomalous supercurrent [59,60]. The anomalous supercurrent density $J_s(\phi = 0)$ for $\Delta_{\text{vp}}/\Delta_s = 3$ can be seen in Fig. 2(e). The $J_s(\phi = 0)$ as a function of valley-polarization strength Δ_{vp} at various temperatures is shown in Fig. 2(f). We find that the anomalous supercurrent is generally finite with valley polarization. Moreover, when $\Delta_{\text{vp}} \gg \Delta_s$, the anomalous current density at the low-temperature range can be as large as tens of nA μm^{-1}. As depicted in Fig. 1(c), we expect to see an anomalous current in a ring geometry when part of the superconducting ring is gated to the valley-polarized state. It is also important to note that unlike previously studied φ_0-JJs, the MATBG φ_0-JJs do not involve ferromagnetism or spin-orbit coupling, which calls for a new understanding about the underlying mechanism for the formation of φ_0-JJs in the MATBG.

IV. UNDERLYING MECHANISM FOR φ_0-JJs IN MATBG

Next, based on the scattering matrix method [74,75], we show analytically that the valley-polarization and the warping effects of moiré bands are crucial in realizing a φ_0-JJ. At the junction, the states can be labeled by the transverse momentum k_y. For illustration, we demonstrate how the Andreev bound state associated with the $k_y = 0$ mode (normal incident states) is affected by valley polarization and the warping terms. The 1D Hamiltonian associated with the $k_y = 0$ mode can be written as $H_{1D} = \sum_{\tau\alpha} \int dx \Psi_{\tau\alpha}^\dagger(x)\hat{H}_{\tau\alpha}(x)\Psi_{\tau\alpha}(x)$. Here, $\tau = +/-$ labels the valley index, $\alpha = +/-$ labels the incoming/outgoing normal states near the Fermi energy, $\Psi_{\tau\nu} = (\psi_{\tau\alpha}(x), \psi_{-\tau,-\alpha}^\dagger(x))^T$ denotes the Nambu basis, and

$$\hat{H}_{\tau\alpha}(x) = \begin{pmatrix} H_{N,\tau\alpha}(x) + \Delta_{\text{vp}}(x)\tau & \Delta_s(x) \\ \Delta_s(x) & H_{N,-\tau-\alpha}^*(x) + \Delta_{\text{vp}}(x)\tau \end{pmatrix}.$$

(4)

Here, the linearized single-particle Hamiltonian $H_{N,\tau\alpha}(x) = -i\alpha\hbar v_{f,\tau\alpha}(x)\partial_x$, and the longitudinal Fermi velocity along the current direction is given by $v_{f,\tau\alpha}$ such that $v_{f,\tau\alpha}(x) = v_{s,\tau\alpha}[\Theta(x) + \Theta(x - d)] + v_{\text{vp},\tau\alpha}\Theta(x)\Theta(d - x)$, where $v_{s,\tau\alpha}$ and $v_{\text{vp},\tau\alpha}$ are the Fermi velocities for the superconducting region and the valley-polarized weak-link region, respectively. Notably, the warping term that breaks the intravalley inversion symmetry could lead to $v_{\text{vp},\tau\alpha} \neq v_{\text{vp},\tau-\alpha}$. The superconducting pairing potential is written as $\Delta_s(x) = \Delta_s(e^{i\frac{\phi}{2}}\Theta(-x) + e^{-i\frac{\phi}{2}}\Theta(x - d))$, and the valley-polarized order parameter is $\Delta_{\text{vp}}(x) = \Delta_{\text{vp}}\Theta(x)\Theta(d - x)$.
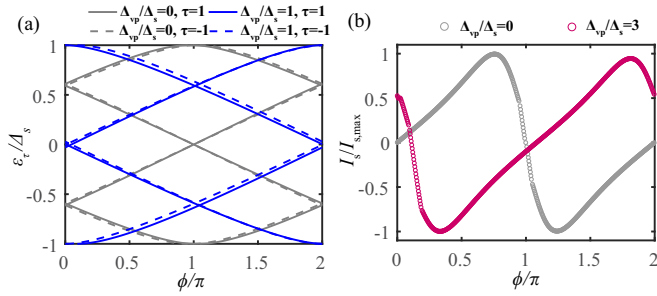
FIG. 3. (a) The energies of the Andreev bound states ϵ_τ vs the phase ϕ obtained from Eq. (5) with $\Delta_{\rm vp}/\Delta_s = 0$ (gray lines) and $\Delta_{\rm vp}/\Delta_s = 1$ (blue lines), where $\tau = \pm 1$ denotes the valley index. (b) The Josephson current I_s (normalized by its maximal value) vs ϕ calculated with the Andreev bound states given by Eq. (5) with $\Delta_{\rm vp}/\Delta_s = 0$ (gray dots) and $\Delta_{\rm vp}/\Delta_s = 3$ (red dots), respectively. The two other energy scales are given by $E_T = 0.65\Delta_s$ and $E_A = 12\Delta_s$, respectively.

With the effective one-dimensional Hamiltonian $H_{\rm 1D}$, we can solve the energies of the Andreev bound states ϵ_τ analytically (τ is a good quantum number), which are given by (for more details, see Appendix B)

$$\cos\left(2\beta - \frac{2(\epsilon_\tau - \tau\Delta_{\rm vp})}{E_T}\right) = \cos\left(\phi + \frac{\epsilon_\tau - \tau\Delta_{\rm vp}}{\tau E_A}\right). \quad (5)$$

Here, $\beta(\epsilon_\tau) = \arccos\frac{\epsilon_\tau}{\Delta_s}$, $E_T = \hbar\bar{v}_{\rm vp}/d$ is the Thouless energy, and $E_A = \hbar\delta\bar{v}_{\rm vp}/d$ is an energy scale that reflects the intravalley asymmetry induced by the warping term, where $\bar{v}_{\rm vp}$ and $\delta\bar{v}_{\rm vp}$ are defined by $\bar{v}_{\rm vp} = 4(\sum_{\tau\nu} v_{{\rm vp},\tau\alpha}^{-1})^{-1}$ and $\delta\bar{v}_{\rm vp} = 2(v_{{\rm vp},++}^{-1} + v_{{\rm vp},--}^{-1} - v_{{\rm vp},+-}^{-1} - v_{{\rm vp},-+}^{-1})^{-1}$.

Importantly, many features of the numerical results as shown in Fig. 2 can be captured by Eq. (5). For example, we can calculate the Andreev bound state energies associated with the $\tau = +/-$ valleys by solving $\epsilon_\tau(\phi)$ from Eq. (5) at $\Delta_{\rm vp}/\Delta_s = 0$ and $\Delta_{\rm vp}/\Delta_s = 1$ [see the gray lines and blue lines in Fig. 3(a), respectively]. Note that in Fig. 3(a), the valley degeneracy of Andreev bound states is lifted by the warping term and valley polarization. With the bound state energies ϵ_τ, it is straightforward to obtain the supercurrent $I_s(\phi)$ by adopting the relation

$$I_s(\phi) = -\frac{2e}{\hbar} \sum_\tau \sum_{\epsilon_\tau > 0} \tanh\left(\frac{\epsilon_\tau}{2k_B T}\right) \frac{\partial \epsilon_\tau}{\partial \phi}. \quad (6)$$

As an illustration, we plot the calculated $I_s(\phi)$ at the low-temperature limit in the cases of $\Delta_{\rm vp}/\Delta_s = 0$ and $\Delta_{\rm vp}/\Delta_s = 3$ [see Fig. 3(b)]. Notably, the features are in agreement with the ones shown in Figs. 2(d) and 2(e).

In the short junction and at the high-temperature limit, we can obtain an analytical form for the Josephson current:

$$I_s(\phi) \approx \frac{e\Delta_s^2}{2\hbar k_B T} \cos\left(\frac{2\Delta_{\rm vp}}{E_T}\right) \sin(\phi - \varphi_0). \quad (7)$$

It can be seen that $I_s(\phi)$ indeed significantly differs from the conventional form given by $I_s(\phi) \propto \sin\phi$. Specifically, the supercurrent exhibits a phase shift $\varphi_0 = \Delta_{\rm vp}/E_A$, which is
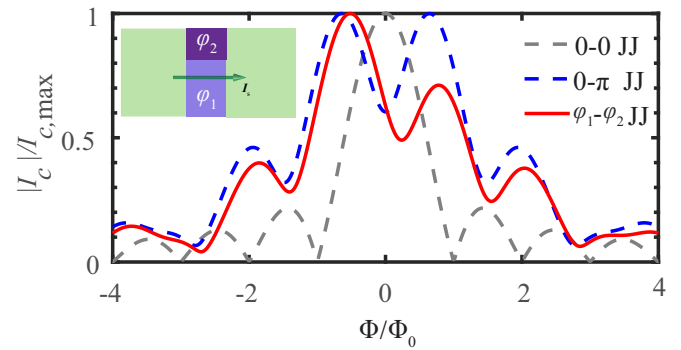

FIG. 4. The Fraunhofer patterns for different types of Josephson junctions. The critical current I_c (normalized by its maximal value) vs the magnetic flux Φ passing through the junction (in units of $\Phi_0 = h/2e$) for the 0-0 (gray), 0-π (blue), and φ_1-φ_2 (red) Josephson junctions, respectively. The inset illustrates a simple two-domain model with different valley-polarization-induced phase shifts φ_1 and φ_2. The Fraunhofer pattern of the φ_1-φ_2 junction matches the experimental observations well with $\varphi_1 = 0.2$, $\varphi_2 = \pi + 0.8$. The widths of the φ_1 and φ_2 sections are chosen to have the ratio $W_{J1}/W_{J2} \approx 2.3$.

determined by both the valley polarization and Fermi velocity asymmetry induced by warping effects ($\varphi_0 = 0$ if there is no asymmetry as $E_A \to \infty$). Remarkably, the factor $\cos(\frac{2\Delta_{\rm vp}}{E_T})$ indicates that the supercurrent oscillates periodically as a function of $\Delta_{\rm vp}$, being consistent with the numerical result in Fig. 2(f). It is worth noting that the results are similar to Eq. (7) for modes with small transverse momentum k_y as well.

V. UNCONVENTIONAL FRAUNHOFER PATTERN

In practice, the sample inhomogeneity and the formations of valley-polarization domain walls may lead to spatially nonuniform $\Delta_{\rm vp}$ inside the weak-link region [76], which can affect the transport properties of the φ_0-JJ. As an illustration, we calculate the Fraunhofer pattern for a simple geometry with two valley-polarization domains (see the inset of Fig. 4), in which each domain generates a phase difference of φ_1 and φ_2, respectively, at the junction. Such a φ_1-φ_2 junction is a generalization of the previously studied 0-π junctions [77–79]. Here, we plot the resulting Fraunhofer patterns in Fig. 4, and the details can be found in Appendix D. Interestingly, the Fraunhofer pattern in the φ_1-φ_2 junction captures the main features found in the recent experiment [41], which exhibits a shift in the central peak, a large asymmetry with respect to the central peak, and a nonvanishing critical current as a function of magnetic fields. These features are not naturally expected by conventional Josephson junctions nor 0-π Josephson junctions [77–79]. It is worth noting that although our study provides a plausible mechanism for the unconventional Fraunhofer pattern seen in the experiment based on φ_0-JJs, we cannot exclude other ways of generating such Fraunhofer patterns. To directly view the φ_0-JJs in the experiment, it would be more straightforward to use the SQUID structures as in previous experiments [67,68], which are discussed in detail in Appendix D.

VI. DISCUSSION

It is important to note that our model exhibits some similarities between the φ_0-JJ model induced by Rashba spin-orbit coupling and exchange field [57,64] by regarding the valley as a pseudospin. Specifically, the trigonal warping term and valley polarization can play the role of spin-orbit coupling and spin polarization, respectively. The detailed mapping is illustrated in Appendix F. This mapping provides a good insight about the appearance of the φ_0-Josephson junction in the MATBG platform, although it is one in which the spin-orbit coupling is negligible. We expect that the φ_0-Josephson is only an example, while other profound physics that typically arises from the interplay of spin-orbit coupling and ferromagnetism can also be explored in the MATBG according to our framework.

In the main text, we focus on the Josephson junction in the ballistic limit. On the other hand, intervalley backscattering can couple the two valleys and effectively weaken the valley polarization and reduce φ_0, similar to the spin-relaxation effects in φ_0-JJ with spin-orbit coupling [64,65,80]. However, as long as the valley polarization is finite, we still expect a φ_0-JJ. Furthermore, our work can be easily extended to study the unconventional Josephson effects mediated by valley-polarized states in other moiré materials/superconductor heterostructures.

ACKNOWLEDGMENTS

APPENDIX A: TRIGONAL WARPING EFFECTS OF MOIRÉ BANDS AND VALLEY-POLARIZED STATES

1. Moiré bands of MATBG and trigonal warping effects

In the main text, the trigonal warping impact of moiré bands and its important effects on creating φ_0-Josephson junctions (JJs) in twisted bilayer graphene is highlighted. Here, we present the details of showing the trigonal warping effects using the continuum model of magic angle twisted bilayer graphene (MATBG) [which is depicted in Fig. 5(a)]. The continuum model of MATBG (cf. [1,4]) can be written as

$$H_\tau(\mathbf{r}) = \begin{pmatrix} H_b(\mathbf{r}) & T(\mathbf{r}) \\ T^\dagger(\mathbf{r}) & H_t(\mathbf{r}) \end{pmatrix}. \qquad (A1)$$

Here, the intralayer moiré Hamiltonian is

$$H_l = -\hbar v R(\theta)\big[(\hat{\mathbf{k}} - \mathbf{K}_\tau^{(l)}) \cdot (\tau\sigma_x, \sigma_y)\big]R^\dagger(\theta), \qquad (A2)$$

where $\hbar v/a = 2.1354$ eV. Here, $l = t/b$ and $\tau = \pm$ label the top/bottom layers and $\pm$ valleys, respectively. The twist angle is denoted as θ, σ_j represent the Pauli matrices defined in the AB sublattice space, $\mathbf{K}_\tau^{(l)}$ labels the Dirac point at
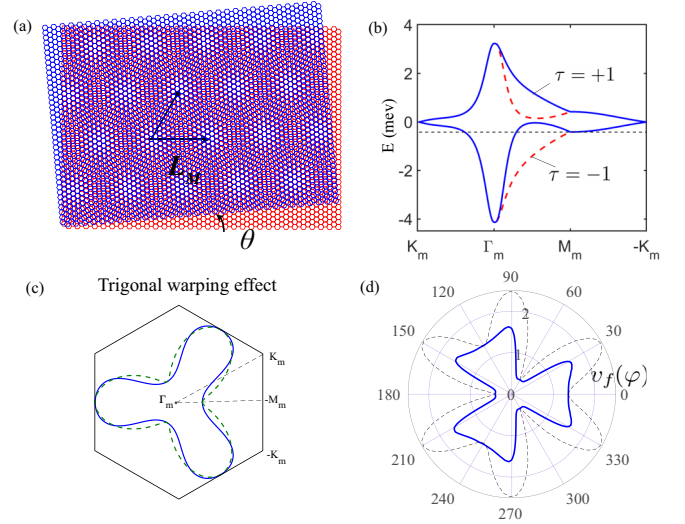

FIG. 5. (a) A schematic plot of the twisted bilayer graphene moiré superlattice (L_M is the lattice constant), which is formed using two layers of graphene with a small twisted angle θ. (b) The lowest moiré bands of twisted bilayer graphene near charge-neutrality points with the magic twist angle $\theta = 1.05°$. The blue/red bands are from $+K/-K$ valley ($\tau = +1/\tau = -1$). Note that we have shifted the charge-neutrality points to be at zero energy. (c) The Fermi contour (in blue) near half-filling [the black dashed line in (a)]. The green dashed line is plotted with $k_f(\varphi) = a + b\cos 3\varphi$. The black solid lines label the moiré Brillouin zone. (d) The blue line shows the anisotropic Fermi velocity along the radical direction $v_f(\varphi)$. The black lines are a plot of $v_f(\varphi)$ estimated using $k_f(\varphi)$. The radius is in units of meV/$\hbar L_M^{-1} \approx 2 \times 10^4$ m/s.

valley τ of the l-layer, and the rotational operator $R(\theta) = \text{diag}(e^{-il\frac{\theta}{2}}, e^{il\frac{\theta}{2}})$. The interlayer Hamiltonian $T(\mathbf{r})$ can be written as

$$T(\mathbf{r}) = \begin{pmatrix} u & u' \\ u' & u \end{pmatrix} + \begin{pmatrix} u & u'e^{-i\omega_\tau} \\ u'e^{i\omega_\tau} & u \end{pmatrix}e^{-i\tau\mathbf{G}_2^M \cdot \mathbf{r}}$$

$$+ \begin{pmatrix} u & u'e^{i\omega_\tau} \\ u'e^{-i\omega_\tau} & u \end{pmatrix}e^{-i\tau\mathbf{G}_3^M \cdot \mathbf{r}}. \qquad (A3)$$

Here, $\omega_\tau = \frac{2\pi}{3}\tau$, $\mathbf{G}_i^M = \frac{4\pi}{\sqrt{3}L_M}(\cos\frac{(i-1)\pi}{3}, \sin\frac{(i-1)\pi}{3})$ with the moiré unit length $L_M = a/\sin\theta \sim 14$ nm, and we adopt $u = 0.0797$ eV, $u' = 0.0975$ eV according to Ref. [4]. The moiré bands can be obtained by diagonalizing the continuum Hamiltonian using the plane-wave basis $\psi_\mathbf{k}(\mathbf{r}) = \sum_\mathbf{G} C_\mathbf{G} e^{i(\mathbf{k}+\mathbf{G})\cdot\mathbf{r}}$ with $G = n_1\mathbf{G}_2^M + n_2\mathbf{G}_3^M$, where n_1, n_2 are integers. Figure 5(b) show the band structure of the lowest moiré bands near the charge-neutrality point of MATBG [4].

To highlight the trigonal warping features of the moiré bands, a Fermi energy contour near half-filling of the $\tau = +1$ valley [the black dashed line in Fig. 5(b)] is plotted in Fig. 5(c) (blue line). We can denote the warped Fermi energy contour as $k_f(\varphi)$. $k_f(\varphi) = k_f(\varphi + \frac{2\pi}{3})$ due to the C_3 symmetry and an emergent C_{2x} symmetry in each valley such that $k_f(\varphi) = k_f(-\varphi)$. To the lowest order in φ, we can expand $k_f(\varphi) \approx a + b\cos 3\varphi$. By using $a = 2.315$, $b = -1.299$ (in unit of L_M^{-1}), we find that $k_f(\varphi)$ can approximately fit the warped Fermi energy contour of the continuum model. The

Fermi energy contour at the $\tau = -1$ valley can be obtained by a time-reversal operation.

Such prominent warping behavior is a direct consequence of the narrow bandwidth and the constraint of D_3 point group symmetry of MATBG [4,5]. Here, we present the symmetry transformation properties under the generators of D_3 which include a threefold rotation along the z-axis and a twofold rotation along the y-axis. Note that the moiré bands are assumed to be decoupled in the valley space so that only the terms that involve τ_0 and τ_z are allowed. Without loss of generality, we consider that the Fermi energy cuts the lower branch of the moiré bands only, as shown in Fig. 5(b). In this case, we can construct a simple symmetry-invariant continuum model near the Γ_m point as

$$H_{\text{eff}} = \lambda_0\left(k_x^2 + k_y^2\right) + \lambda_1 k_x\left(k_x^2 - 3k_y^2\right)\tau_z - \mu. \quad (A4)$$

Here, the first term is the kinetic energy term, μ denotes the chemical potential term, and the second term is the warping term, which is opposite at the opposite valley to preserve the time-reversal symmetry $T = \tau_x K$ and $C_{2y} = \tau_x$ symmetry. The presence of the warping term breaks the intravalley inversion symmetry as $I_0 H_{\text{eff}}(\mathbf{k})I_0^{-1} \neq H_{\text{eff}}(-\mathbf{k})$, where under $I_0 : \tau \mapsto \tau, \mathbf{k} \mapsto -\mathbf{k}$. As emphasized in the main text, the breaking of intravalley inversion symmetry together with the valley polarization enables the generation of the φ_0-Josephson effect in MATBG even in the absence of the spin-orbit coupling.

One of the important consequences of the warping effects is to enable the velocity of incoming and outgoing states in the junction to be asymmetric, which plays a crucial role in creating a nontrivial φ_0 as shown in later sections. To show the asymmetry of the Fermi velocity in the moiré bands, we plot the angular dependence of Fermi velocity $v_f(\varphi)$ [see the blue line in Fig. 5(d), in units of meV/$\hbar L_M^{-1}$], which is defined as $v_f(\varphi) = \sqrt{v_x[k_f(\varphi)]^2 + v_y[k_f(\varphi)]^2}$, where $k_f(\varphi)$ is the Fermi momentum contour as shown in Fig. 5(c). In other words, $v_f(\varphi)$ is the Fermi velocity along the radical direction at each φ. For normal incident states, we can estimate that the asymmetry of the Fermi velocity is given by $v_f(\varphi{=}0) - v_f(\varphi = \pi) \approx$ meV/$\hbar L_M^{-1} \approx 2 \times 10^4$ m/s. Note that the Fermi velocity is two orders smaller than that of monolayer graphene due to the formation of flat bands under a moiré superlattice potential.

To highlight the anisotropy of Fermi velocity induced by the warping term in Eq. (A4), we can rewrite the H_{eff} in polar coordinates as $H_{\text{eff}}(k_r) = \lambda_0 k_r^2 + \lambda_1 k_r^3 \cos(3\varphi)\tau_z - \mu$. For the $\tau = +1$ valley, the $v_f(\varphi)$ can be obtained as $v_f(\varphi) = \frac{\partial H_{\text{eff}}(k_f(\varphi))}{\partial k_r} = 2\lambda_0 k_f(\varphi) + 3\lambda_1 k_f^2(\varphi)\cos(3\varphi)$. Inserting $k_f(\varphi) \approx a + b \cos 3\varphi$, the form of $v_f(\varphi)$ is obtained. We made a plot of $v_f(\varphi)$ with parameters $\lambda_0 = 0.5347$ and $\lambda_1 = 0.0885$ [see the dashed line in Fig. 5(d)]. Although there is some deviation from the numerical one (in blue), all the symmetry features are captured. To obtain a closer fitting to the numerical results, one can expand it to higher-order terms, which is not necessary for the purposes of this manuscript. Therefore, we have shown that the trigonal warping effects would result in anisotropic Fermi velocities. The warping term would induce an asymmetry for the velocities of the

incoming and outgoing modes in our scattering matrix method calculations later.

2. An illustration of valley-polarized states from the Hartree-Fock mean-field approximation

A more detailed Hartree-Fock mean-field approximation for the moiré bands upon Coulomb interaction has been extensively studied in previous works. However, for the sake of completeness, and to illustrate some features of the moiré bands upon the valley-polarization, we present the basic formalisms of the valley-polarized states from the Hartree-Fock approximation with a minimal interacting Hamiltonian:

$$H_0 = \sum_{\mathbf{k},\tau,s}(\epsilon_{\mathbf{k},\tau} - \mu)\psi_{\mathbf{k},\tau,s}^{\dagger}\psi_{\mathbf{k},\tau,s} + \frac{1}{2A}\sum_{\mathbf{q}} V_{\mathbf{q}} : \rho_{\mathbf{q}}\rho_{-\mathbf{q}} : . \quad (A5)$$

Here, A is the sample area, s denotes the spin index, μ is the chemical potential for the single-particle moiré band, and the density operator $\rho_{\mathbf{q}} = \sum_{\mathbf{k},\mathbf{k}',\tau,s}\langle c_{\mathbf{k},\tau,s}|e^{i\mathbf{q}\cdot\mathbf{r}}|c_{\mathbf{k}',\tau,s}\rangle c_{\mathbf{k},\tau,s}^{\dagger}c_{\mathbf{k}',\tau,s}$. Without loss of generality, we focus on the first valence moiré band, and the Coulomb interaction is projected to this moiré band [71]. The singlet-particle wave function can be decomposed into the plane-wave basis as $|c_{\mathbf{k},\tau,s}\rangle = \frac{1}{\sqrt{A}}\sum_{\mathbf{G}} a_{\mathbf{k}+\mathbf{G},\tau,s}e^{i(\mathbf{k}+\mathbf{G})\cdot\mathbf{r}}$, with $\mathbf{G}$ being the moiré reciprocal-lattice vector.

The Hartree-Fock mean-field Hamiltonian with a spin- and valley-polarized ground state can be written as

$$H_0^{\text{HF}} \approx \sum_{\mathbf{k},\tau} E_{\mathbf{k},\tau,s}\psi_{\mathbf{k},\tau,s}^{\dagger}\psi_{\mathbf{k},\tau,s}, \quad (A6)$$

where

$$E_{\mathbf{k},\tau,s} = (\epsilon_{\mathbf{k},\tau} - \mu) + \Delta_{\mathbf{k},\tau,s}, \quad (A7)$$

$$\Delta_{\mathbf{k},\tau,s} = \frac{1}{A}\sum_{\mathbf{k}',\tau',s'} V_{\mathbf{k}\mathbf{k}'\mathbf{k}'\mathbf{k},ss's's}^{\tau\tau'\tau'\tau}n_F(E_{\mathbf{k}',\tau',s'})$$

$$- \frac{1}{A}\sum_{\mathbf{k}'} V_{\mathbf{k}\mathbf{k}'\mathbf{k}\mathbf{k}',ssss}^{\tau\tau\tau\tau}n_F(E_{\mathbf{k}',\tau,s}). \quad (A8)$$

Here, n_F is the Fermi-Dirac occupation function, the first term on the right-hand side of Eq. (A8) is the Hartree energy, while the second term is the Fock energy. The Coulomb interaction strength is written as

$$V_{\mathbf{k}_1\mathbf{k}_2\mathbf{k}_3\mathbf{k}_4,ss's's}^{\tau\tau'\tau'\tau} = \sum_{\mathbf{q}} V_{\mathbf{q}}\langle c_{\mathbf{k}_1,\tau,s}|e^{i\mathbf{q}\cdot\mathbf{r}}|c_{\mathbf{k}_4,\tau,s}\rangle$$

$$\times \langle c_{\mathbf{k}_2,\tau',s'}|e^{-i\mathbf{q}\cdot\mathbf{r}}|c_{\mathbf{k}_3,\tau',s'}\rangle$$

$$= \sum_{\mathbf{q},\mathbf{G}_1,\mathbf{G}_2,\mathbf{G}_3,\mathbf{G}_4} V_{\mathbf{q}}a_{\mathbf{k}_1+\mathbf{G}_1,\tau,s}^{*}a_{\mathbf{k}_2+\mathbf{G}_2,\tau',s'}^{*}a_{\mathbf{k}_3+\mathbf{G}_3,\tau',s'}$$

$$\times a_{\mathbf{k}_4+\mathbf{G}_4,\tau,s}\delta_{\mathbf{k}_1+\mathbf{G}_1,\mathbf{q}+\mathbf{k}_4+\mathbf{G}_4}\delta_{\mathbf{k}_3+\mathbf{G}_3,\mathbf{q}+\mathbf{k}_2+\mathbf{G}_2}. \quad (A9)$$

Hence, the Coulomb interactions in the Hartree term and the Fock term are written as

$$V_{\mathbf{k}\mathbf{k}'\mathbf{k}'\mathbf{k},ss's's}^{\tau\tau'\tau'\tau} = \sum_{\mathbf{q},\mathbf{G}_1,\mathbf{G}_2,\mathbf{G}_3,\mathbf{G}_4} V_{\mathbf{q}}a_{\mathbf{k}+\mathbf{G}_1,\tau,s}^{*}a_{\mathbf{k}'+\mathbf{G}_2,\tau',s'}^{*}$$

$$\times a_{\mathbf{k}'+\mathbf{G}_3,\tau',s'}a_{\mathbf{k}+\mathbf{G}_4,\tau,s}\delta_{\mathbf{G}_1,\mathbf{q}+\mathbf{G}_4}\delta_{\mathbf{G}_3,\mathbf{q}+\mathbf{G}_2}, \quad (A10)$$

$$V_{\mathbf{kk'kk'},ssss}^{\tau\tau\tau\tau} = \sum_{\mathbf{q},\mathbf{G_1},\mathbf{G_2},\mathbf{G_3},\mathbf{G_4}} V_{\mathbf{q}} a_{\mathbf{k}+\mathbf{G_1},\tau,s}^* a_{\mathbf{k'}+\mathbf{G_2},\tau,s}^* a_{\mathbf{k}+\mathbf{G_3},\tau,s}$$

$$\times\, a_{\mathbf{k'}+\mathbf{G_4},\tau,s} \delta_{\mathbf{k}+\mathbf{G_1},\mathbf{q}+\mathbf{k'}+\mathbf{G_4}} \delta_{\mathbf{k}+\mathbf{G_3},\mathbf{q}+\mathbf{k'}+\mathbf{G_2}}. \quad (A11)$$

One can solve Eq. (A8) in a self-consistent way. Note that the doubly counted interacting energy should be subtracted after the mean-field approximation, which is given by

$$E_0 = \frac{1}{2A} \sum_{\mathbf{k},\mathbf{k'},\tau,\tau',s,s'} \left[V_{\mathbf{kk'k'k},ss's's}^{\tau\tau'\tau'\tau} - V_{\mathbf{kk'kk'},ss's's}^{\tau\tau'\tau'\tau} \right.$$

$$\left. \times\, \delta_{\tau,\tau'} \delta_{s,s'} \right] n_F(E_{\mathbf{k},\tau,s}) n_F(E_{\mathbf{k'},\tau',s'}). \quad (A12)$$

Depending on the filling and the Coulomb interaction strength, various time-reversal breaking states with valley-polarization that satisfy the self-consistent Hartree-Fock equation can be obtained, including the following: (i) The fully valley-polarized, spin-unpolarized insulating or semimetallic state. This state can appear when the Coulomb interaction strength is strong and the filling factor is near some integer fillings. (ii) The partially valley-polarized, spin-unpolarized metallic states, which can appear when the Coulomb interactions are weaker [31]. (iii) The valley-polarized, spin-polarized states. A schematic illustration of the valley-polarized states is presented in the main text (Fig. 1). As the focus of this work is the valley-polarized state, we neglect the spin polarization and rewrite the mean-field Hamiltonian as

$$H_0^{\text{HF}} \approx \sum_{\mathbf{k},\tau} \psi_{\mathbf{k},\tau}^\dagger [(\tilde{\epsilon}_{\mathbf{k},\tau} - \mu) + \Delta_{\text{vp},\mathbf{k}} \tau_z] \psi_{\mathbf{k},\tau}, \quad (A13)$$

where $\tilde{\epsilon}_{\mathbf{k},\tau} = \epsilon_{\mathbf{k},\tau} + (\Delta_{\mathbf{k},\tau} + \Delta_{\mathbf{k},-\tau})/2$ and $\Delta_{\text{vp},\mathbf{k}} = (\Delta_{\mathbf{k},\tau} - \Delta_{\mathbf{k},-\tau})/2$, and $\Delta_{\text{vp}}\tau_z$ is the valley-polarized order parameter. Note that here we are directly taking the valley-polarized state as the ansatz state. It is actually difficult to determine which state is more energetically favorable based on Hartree-Fock consideration alone. Especially when the correlated state appears at the weak-link region, the coupling with the superconducting regions can also be important.

APPENDIX B: ANALYTICAL CALCULATIONS OF THE CURRENT-PHASE RELATION USING THE SCATTERING MATRIX METHOD

In the main text, we have used the scattering matrix method to show that the studied MATBG Josephson junction is a φ_0-JJ, and we find that the valley polarization and warping effects are crucial in giving rise to the observed φ_0-JJ. We present the corresponding details in this Appendix.

1. Model Hamiltonian

To gain some insight into the crucial features of the junction, we first look at the limit of $\Delta_s, \Delta_{\text{vp}} \ll \mu$, i.e., the bandwidth is the biggest energy scale. In this case, we can linearize the momentum near Fermi energy for a fixed transverse momentum k_y and obtain a low-energy effective model as

$$H = \frac{1}{2} \sum_{\tau\alpha} \sum_{k_y} \int dx \Psi_{k_y,\tau\alpha}^\dagger(x) \hat{H}_{k_y,\tau\alpha}(x) \Psi_{k_y,\tau\alpha}(x). \quad (B1)$$

Here, $\tau\pm$ labels the $\pm K$ valley, $\alpha = +/-$ labels the incoming/outgoing normal states near the Fermi energy, $\Psi_{k_y,\tau\alpha} = (\psi_{k_y,\tau\alpha}(x), \psi_{k_y,-\tau,-\alpha}^\dagger(x))^T$ denotes the Nambu basis, and

$$\hat{H}_{\tau\alpha}(x) = \begin{pmatrix} -i\alpha\hbar v_{f,\tau\alpha}(k_y,x)\partial_x + \Delta_{\text{vp}}(x)\tau & \Delta_s(x) \\ \Delta_s(x) & i\alpha\hbar v_{f,-\tau-\alpha}(k_y,x)\partial_x + \Delta_{\text{vp}}(x)\tau \end{pmatrix} \quad (B2)$$

with the pairing potential $\Delta_s(x) = \Delta_s[e^{i\frac{\phi}{2}}\theta(-x) + e^{-i\frac{\phi}{2}}\theta(x - d)]$, valley polarization $\Delta_{\text{vp}}(x) = \Delta_{\text{vp}}\theta(x)\theta(d - x)$ (note that here, we have assumed a uniform valley polarization for the sake of simplicity), and the longitudinal Fermi velocity at a fixed k_y of the superconducting part and the junction part is given by $v_{f,\tau\alpha}(k_y,x) = v_{s,\tau\alpha}(k_y)[\theta(-x) + \theta(x - d)] + v_{\text{vp},\tau\alpha}(k_y)\theta(x)\theta(d - x)$ [for the compact of notations, we will denote $v_{f,\tau\alpha}(k_y,x) \equiv v_{f,\tau\alpha}(x)$ in the following]. Here, ϕ is the phase difference, d is the length of the junction, Δ_{vp} is the valley polarization strength, and $v_{s,\tau\alpha}$, $v_{f,\tau\alpha}$ are the longitudinal Fermi momentum along the current direction of the superconducting part and the junction part with valley polarization. One can verify that the whole Hamiltonian $\hat{H}$ (dimension is 8 by 8) preserves particle-hole symmetry $P\hat{H}P^{-1} = -\hat{H}$ but breaks time-reversal symmetry $T\hat{H}T^{-1} \neq \hat{H}$ if Δ_{vp} is finite. Here, $\hat{P} = \rho_x\alpha_x\tau_x\hat{K}$, $\hat{T} = \alpha_x\tau_x\hat{K}$, $\hat{K}$ is a complex conjugate, α_j, $\hat{K}$ is com τ_j, and ρ_j are Pauli matrices defined in $\alpha = +/-$, valley, and particle-hole space, respectively.

Note that in general $v_{\text{vp},\tau\alpha} \neq v_{\text{vp},-\tau-\alpha}$ due to the breaking of time-reversal symmetry, but $v_{\text{vp},\tau\alpha} \approx v_{\text{vp},-\tau-\alpha}$ in the limit

of $\Delta_{\text{vp}} \ll E_F'$. On the other hand, the warping term breaking intravalley time-reversal symmetry could lead to $v_{\text{vp},\tau\alpha} \neq v_{\text{vp},\tau-\alpha}$, which plays a crucial role in giving rise to the φ_0 junction as shown later.

It is worth noting that the model Hamiltonian resembles that for an S/F/S junction if the valley is regarded as a pseudospin (flips sign under both time-reversal and inversion operation). As we will show later, the π junction, which was commonly explored in S/F/S junctions, can also be stabilized in S/VP/S junctions. But we would emphasize that the physics system in our case is very different, given that the polarization appears in valley degree of freedom rather than spin.

2. Scattering states and boundary conditions

The scattering states in the S region of the left (L) and right (R) side are obtained as

$$\psi_{s,\tau\alpha}^L = \begin{pmatrix} e^{-i\alpha\beta} \\ e^{-i\frac{\phi}{2}} \end{pmatrix} e^{i\alpha k_{s,\tau\alpha}^0 x + \kappa_{\tau\alpha}x + ik_y y}, \; x \leqslant 0, \quad (B3)$$

The scattering state in the VP region ($0 \leqslant x \leqslant d$) is

$$\psi_{\mathrm{vp},e,\tau\alpha} = \frac{1}{\sqrt{N_{e,\tau\alpha}}}\begin{pmatrix}1\\0\end{pmatrix}e^{ik_{e,\tau\alpha}x+ik_y y}, \tag{B7}$$

$$\psi_{\mathrm{vp},h,\tau\alpha} = \frac{1}{\sqrt{N_{h,\tau\alpha}}}\begin{pmatrix}0\\1\end{pmatrix}e^{ik_{h,\tau\alpha}x+ik_y y}. \tag{B8}$$

Here, $k_{e,\tau\alpha}$ and $k_{h,\tau\alpha}$ are the wave vectors for electron- and holelike states, respectively (see an illustration in Fig. 6), and $N_{e(h),\tau\alpha}$ are normalization factors to ensure that the scattering matrices are unitary. Up to leading order, $k_{e,\tau\alpha} \approx k^0_{e,\tau\alpha} + \delta k_{e,\tau\alpha}$, $k_{h,\tau\alpha} \approx k^0_{h,\tau\alpha} + \delta k_{h,\tau\alpha}$ with $k^0_{e,\tau\alpha} = k^0_{h,\tau\alpha} = \alpha k^0_{\mathrm{vp},\tau\alpha}$, and

$$\delta k_{e,\tau\alpha} = \frac{\epsilon - \tau\Delta_{\mathrm{vp}}}{\alpha\hbar v_{\mathrm{vp},\tau\alpha}}, \tag{B9}$$

$$\delta k_{h,\tau\alpha} = -\frac{\epsilon - \tau\Delta_{\mathrm{vp}}}{\alpha\hbar v_{\mathrm{vp},-\tau-\alpha}}. \tag{B10}$$

Here, $\psi_{\mathrm{vp},e,\tau+}$, $\psi_{\mathrm{vp},h,\tau-}$ are the states moving in the $+x$ direction, while $\psi_{\mathrm{vp},e,\tau-}$, $\psi_{\mathrm{vp},h,\tau+}$ are the states moving in the $-x$ direction. The particle-hole symmetry requires $\psi_{\mathrm{vp},h}(-\epsilon) = \hat{P}\psi_{\mathrm{vp},e}(\epsilon)$ so that $\delta k_{h,\tau\alpha}(-\epsilon) = -\delta k_{e,-\tau-\alpha}(\epsilon)$. The factors $\sqrt{N_{e,\tau\alpha}}$ and $\sqrt{N_{h,\tau\alpha}}$ are to ensure that the scattering matrix is unitary.

As $\hat{H}$ is block-diagonalized in the valley space with $[\tau_z, \hat{H}] = 0$, we can solve the scattering matrix for $\tau = +$ and $\tau = -$ separately. We also assume that the transverse momentum k_y is conserved during the scatterings. The boundary conditions at $x = 0$ and $x = d$ are
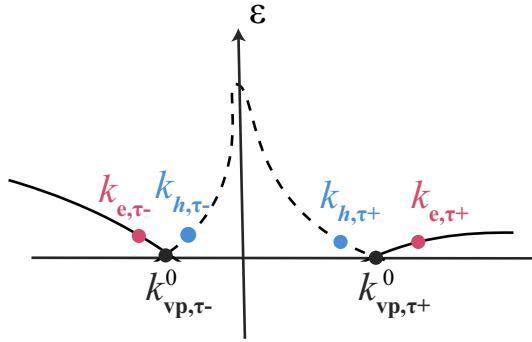

FIG. 6. A schematic plot of the wave vectors $k_{e(h),\tau\alpha}$ on the quasi-particle excitation. The electron- and holelike quasiparticle bands are highlighted with a solid line and a dashed line, respectively.

$$\psi^R_{s,\tau\alpha} = \begin{pmatrix}e^{i\alpha\beta}\\e^{i\frac{\phi}{2}}\end{pmatrix}e^{i\alpha k^0_{s,\tau\alpha}(x-L)-\kappa_{\tau\alpha}(x-L)+ik_y y}, \quad x \geqslant d, \tag{B4}$$

with $k^0_{s,\tau\alpha}$ being the Fermi momentum along the longitudinal direction for a fixed k_y and the definitions

$$\kappa_{\tau\alpha} = \frac{\sqrt{\Delta^2_s - \epsilon^2}}{\hbar v_{s,\tau\alpha}}, \tag{B5}$$

$$\beta = \begin{cases}\mathrm{acos}\frac{\epsilon}{\Delta_s} & \text{if } \epsilon < \Delta_s, \\ -i\,\mathrm{acosh}\frac{\epsilon}{\Delta_s} & \text{if } \epsilon > \Delta_s.\end{cases} \tag{B6}$$

The in-gap states $\psi^{L/R}_{s,\tau\alpha}$ with $\epsilon \lesssim \Delta_s$ are superpositions of electron and hole with an exponential decay length $\kappa^{-1}_{\tau\alpha}$ into the left/right superconducting regions. One can verify that the states in the S region possess time-reversal symmetry: $\psi_s(\epsilon, -\phi) = \hat{T}\psi_s(\epsilon, \phi)$ with $k^0_{s,\tau\alpha} = k^0_{s,-\tau-\alpha}$.

$$a\psi^L_{s,\tau+}(x=0) + b\psi^L_{s,\tau-}(x=0) = c^+_e\psi_{\mathrm{vp},e,\tau+}(x=0) + c^-_e\psi_{\mathrm{vp},e,\tau-}(x=0) + c^+_h\psi_{\mathrm{vp},h,\tau+}(x=0) + c^-_h\psi_{\mathrm{vp},h,\tau-}(x=0), \tag{B11}$$

$$a'\psi^R_{s,\tau+}(x=d) + b'\psi^R_{s,\tau-}(x=d) = c^+_e\psi_{\mathrm{vp},e,\tau+}(x=d) + c^-_e\psi_{\mathrm{vp},e,\tau-}(x=d) + c^+_h\psi_{\mathrm{vp},h,\tau+}(x=d) + c^-_h\psi_{\mathrm{vp},h,\tau-}(x=d), \tag{B12}$$

$$av_{s,\tau+}\psi^L_{s,\tau+}(x=0) + bv_{s,\tau-}\psi^L_{s,\tau-}(x=0) = v_{\mathrm{vp},\tau+}c^+_e\psi_{\mathrm{vp},e,\tau+}(x=0) - v_{\mathrm{vp},\tau-}c^-_e\psi_{\mathrm{vp},e,\tau-}(x=0)$$
$$+ v_{\mathrm{vp},-\tau-}c^+_h\psi_{\mathrm{vp},h,\tau+}(x=0) - v_{\mathrm{vp},-\tau+}c^-_h\psi_{\mathrm{vp},h,\tau-}(x=0), \tag{B13}$$

$$a'v_{s,\tau+}k_{0,\tau+}\psi^R_{s,\tau+}(x=d) - b'v_{s,\tau-}\psi^R_{s,\tau-}(x=d) = v_{\mathrm{vp},\tau+}c^+_e\psi_{\mathrm{vp},e,\tau+}(x=d) - v_{\mathrm{vp},\tau-}c^-_e\psi_{\mathrm{vp},e,\tau-}(x=d)$$
$$+ v_{\mathrm{vp},-\tau-}c^+_h\psi_{\mathrm{vp},h,\tau+}(x=d) - v_{\mathrm{vp},-\tau+}c^-_h\psi_{\mathrm{vp},h,\tau-}(x=d). \tag{B14}$$

Here, Eqs. (B11) and (B12) are obtained from the continuity of the wave function, while Eqs. (B13) and (B14) are obtained from the conservation of particle current, which for each state is given by $\mathrm{Im}(\langle\psi|\frac{\partial H_{\tau\alpha}(\mathbf{r})}{\partial p_x}|\psi\rangle) = \langle\psi|\mathrm{diag}(\alpha v_{f,\tau\alpha}, -\alpha v_{f,-\tau-\alpha})|\psi\rangle$.

3. Andreev bound states in the case without normal reflections

We now solve the Andreev bound states using the scattering matrix method [74,75]. First, we need to work out the scattering matrices. We can define

$$a(L) = a, \quad b(L) = b, \quad a(R) = a', \quad b(R) = b'; \tag{B15}$$

$$c^\dagger_e(L) = c^+_e, \quad c^-_e(L) = c^-_e, \quad c^+_h(L) = c^+_h, \quad c^-_h(L) = c^-_h; \tag{B16}$$

$$c^\dagger_e(R) = c^+_e e^{i(k^0_{e,\tau+}+\delta k_{e,\tau+})d}, \quad c^-_e(R) = c^-_e e^{i(k^0_{e,\tau-}+\delta k_{e,\tau-})d}; \tag{B17}$$

$$c^+_h(R) = c^+_h e^{i(k^0_{h,\tau+}+\delta k_{h,\tau+})d}, \quad c^-_h(R) = c^-_h e^{i(k^0_{h,\tau-}+\delta k_{h,\tau-})d}. \tag{B18}$$

The scattering matrices in the scattering method are defined as

$$\begin{pmatrix} c_e^+(L) \\ c_h^-(L) \end{pmatrix} = S_L \begin{pmatrix} c_e^-(L) \\ c_h^+(L) \end{pmatrix}, \quad \begin{pmatrix} c_e^-(R) \\ c_h^+(R) \end{pmatrix} = S_R \begin{pmatrix} c_e^+(R) \\ c_h^-(R) \end{pmatrix}, \quad \text{(B19)}$$

and the transition matrices are defined as

$$\begin{pmatrix} c_e^+(R) \\ c_h^-(R) \end{pmatrix} = T_{RL} \begin{pmatrix} c_e^+(L) \\ c_h^-(L) \end{pmatrix}, \quad \begin{pmatrix} c_e^-(L) \\ c_h^+(L) \end{pmatrix} = T_{LR} \begin{pmatrix} c_e^-(R) \\ c_h^+(R) \end{pmatrix}. \quad \text{(B20)}$$

According to the scattering matrix method [74,75], the energies of Andreev bound states are given by

$$\text{Det}[1 - T_{LR} S_R T_{RL} S_L] = 0. \quad \text{(B21)}$$

The transmission matrices can be directly obtained according to the definitions Eqs. (B15)–(B18) and Eq. (B20) as

$$T_{RL} = \begin{pmatrix} e^{i(k_{e,\tau+}^0 + \delta k_{e,\tau+})d} & 0 \\ 0 & e^{i(k_{h,\tau-}^0 + \delta k_{h,\tau-})d} \end{pmatrix}, \quad \text{(B22)}$$

$$T_{LR} = \begin{pmatrix} e^{-i(k_{e,\tau-}^0 + \delta k_{e,\tau-})d} & 0 \\ 0 & e^{-i(k_{h,\tau+}^0 + \delta k_{h,\tau+})d} \end{pmatrix}. \quad \text{(B23)}$$

The form of the scattering matrix $S_{L(R)}$ would depend on the interface at $x = 0$ and $x = d$. Let us first consider the case without a chemical potential difference between the superconducting region and the valley-polarized region, i.e., $\mu = \mu'$. In this case, $v_{\text{vp},\tau\pm} = v_{s,\tau\pm}$, the factors in the scattering states can be simply taken as $N_{e,\tau\alpha} = N_{h,\tau\alpha} = 1$. Using the definitions Eqs. (B15)–(B18) and the boundary conditions Eqs. (B11)–(B14), one can easily obtain

$$S_{L(R)} = \begin{pmatrix} 0 & e^{\pm i\frac{\phi}{2} - i\beta} \\ e^{\mp i\frac{\phi}{2} - i\beta} & 0 \end{pmatrix}. \quad \text{(B24)}$$

Here, $\beta = \text{acos}\frac{\epsilon_\tau}{\Delta_s}$ for in-gap Andreev bound states, and only Andreev reflections in the scattering matrix are finite due to the absence of momentum mismatches. By inserting the scattering matrix back to Eq. (B21), we find that the energies of Andreev bound states are given by

$$\cos\left(2\beta - \frac{2(\epsilon_\tau - \tau\Delta_{\text{vp}})d}{\hbar\bar{v}_{\text{vp}}}\right) = \cos\left(\phi + \frac{(\epsilon_\tau - \tau\Delta_{\text{vp}})d}{\tau\hbar\delta v_{\text{vp}}}\right), \quad \text{(B25)}$$

where

$$\bar{v}_{\text{vp}} = \frac{4}{\sum_{\tau\alpha} v_{\text{vp},\tau\alpha}^{-1}}, \quad \text{(B26)}$$

$$\delta\bar{v}_{\text{vp}} = \frac{2}{v_{\text{vp},++}^{-1} + v_{\text{vp},--}^{-1} - v_{\text{vp},+-}^{-1} - v_{\text{vp},-+}^{-1}}. \quad \text{(B27)}$$

We can further define two energy scales: one is the Thouless energy $E_T = \hbar\bar{v}_{\text{vp}}/d$, and the other one is $E_A = \hbar\delta\bar{v}_{\text{vp}}/d$, which reflects the intravalley asymmetry induced by the warping term. Then Eq. (B25) is rewritten as

$$\cos\left(2\beta - \frac{2(\epsilon_\tau - \tau\Delta_{\text{vp}})}{E_T}\right) = \cos\left(\phi + \frac{\epsilon_\tau - \tau\Delta_{\text{vp}}}{\tau E_A}\right). \quad \text{(B28)}$$

It clearly shows that the phase ϕ is shifted as $\tilde{\phi} = \phi - \varphi_0$ with

$$\varphi_0 = \Delta_{\text{vp}}/E_A \quad \text{(B29)}$$

due to the combination of valley polarization and warping effects. As we will see later, φ_0 would manifest as the phase shift in a current-phase relation, which would result in the so-called φ_0 junction. In the short junction limit, $\epsilon \ll E_A, E_T$, we can actually obtain the energies of the bound states:

$$\epsilon_\tau = \Delta_s \sqrt{1 - \sin^2\left(\frac{\tilde{\phi}}{2} - \frac{\tau\Delta_{\text{vp}}}{E_T}\right)}. \quad \text{(B30)}$$

4. Angular dependence of the φ_0 phase shift

Next, we briefly comment on the angular dependence of the φ_0 phase shift. It is important to note that the magnitude of φ_0 in general would depend on the angle θ between the current direction and the lattice orientation. As an illustration, we can evaluate the φ_0 phase shift with the approximated angular dependence of the Fermi velocity presented in Sec. I: $v_f(\theta) = \alpha_0 + \beta_0 \tau \cos 3\theta$, where τ is the valley index, α_0 captures the isotropic part, and β_0 captures the anisotropic part of the Fermi velocity. It is straightforward to obtain φ_0 according to the relation between E_A and $v_f(\theta)$, which gives

$$\varphi_0(\theta) = \frac{2\beta_0 \cos(3\theta)d\Delta_{\text{vp}}}{\hbar(\beta_0^2 \cos^2 3\theta - \alpha^2)}. \quad \text{(B31)}$$

Therefore, it can be seen that the φ_0 phase shift would exhibit a threefold symmetry: $\varphi_0(\theta) = \varphi_0(\theta + \frac{2\pi}{3})$, depending on the lattice orientation and the current direction.

5. Andreev bound states in the case with normal reflections

In general, the chemical potential between the superconducting region and the valley-polarized region is different with $\mu \neq \mu'$. To see the effects of such a difference in chemical potential, we solved the scattering matrices in the same way as

$$S_{L(R)} = \begin{pmatrix} r_N & r_A e^{\pm i\frac{\phi}{2} - i\beta} \\ r_A e^{\mp i\frac{\phi}{2} - i\beta} & r_N \end{pmatrix} \quad \text{(B32)}$$

with

$$r_A = e^{i\beta} X^{-1} (v_{\text{vp},\tau+} + v_{\text{vp},\tau-})(v_{s,\tau+} + v_{s,\tau-}), \quad \text{(B33)}$$

$$r_N = 2i X^{-1} \sin\beta \sqrt{(v_{\text{vp},\tau+} + v_{s,\tau-})(v_{\text{vp},\tau-} + v_{s,\tau+})(v_{\text{vp},\tau+} - v_{s,\tau+})(v_{\text{vp},\tau-} - v_{s,\tau-})}, \quad \text{(B34)}$$

$$X = e^{i\beta}(v_{\text{vp},\tau+} + v_{s,\tau-})(v_{\text{vp},\tau-} + v_{s,\tau+}) - e^{-i\beta}(v_{\text{vp},\tau+} - v_{s,\tau+})(v_{\text{vp},\tau-} - v_{s,\tau-}). \quad \text{(B35)}$$

Here, r_A, r_N are coefficients for Andreev reflections and normal reflections. Note that we have used $N_{e,\tau+} = N_{h,\tau+} = \sqrt{(v_{vp,\tau+} - v_{s,\tau+})(v_{vp,\tau+} + v_{s,\tau-})}$, $N_{e,\tau-} = N_{h,\tau-} = \sqrt{(v_{vp,\tau-} - v_{s,\tau-})(v_{vp,\tau-} + v_{s,\tau+})}$. One can verify that the scattering matrix is unitary with $|r_A|^2 + |r_N|^2 = 1$ for the in-gap bound states with $\epsilon < \Delta$. Evidently, the normal reflections r_N would be finite due to the momentum mismatches, i.e., $v_{vp,\tau\pm} \neq v_{s,\tau\pm}$ induced by the difference in the chemical potential ($\mu \neq \mu'$). It can also be seen that the scattering matrix Eq. (B32) would return to Eq. (B24) if there were no momentum mismatch.

Next, we solve the energies of Andreev bound states in the case of finite normal reflections. For the compact of notations, we rewrite the scattering matrix as

$$S_{L(R)} = \begin{pmatrix} ire^{i\eta} & \sqrt{1-r^2}e^{i\eta} \\ \sqrt{1-r^2}e^{i\eta} & ire^{i\eta} \end{pmatrix}. \qquad (B36)$$

Here, $r = |r_N|$, $\eta = \text{Arg}[X^{-1}]$. By substituting the scattering back to Eq. (B21), we find that the Andreev bound states are given by

$$\cos\left(2\eta + \frac{2(\epsilon - \tau\Delta_{vp})}{E_T}\right) + r^2 \cos\left(\sum_\alpha k_{\tau\alpha}^0\right)$$
$$= (1 - r^2)\cos\left(\phi + \frac{\epsilon - \tau\Delta_{vp}}{\tau E_A}\right). \qquad (B37)$$

As expected, the phase shift $\varphi_0 = \frac{\Delta_{vp}}{E_A}$ would not be affected by the presence of normal reflections. Instead, the normal reflection would mainly weaken the magnitude of the supercurrent and thus is not essential for our study.

6. Free energy and Josephson currents

The free energy of a JJ can be written as

$$F = \int d\mathbf{r} \frac{|\Delta_s|^2}{U} - \frac{1}{\beta}\sum_{\epsilon_n} \ln(1 + e^{-\beta\epsilon_n}), \qquad (B38)$$

where ϵ_n are the eigenenergies of the BdG Hamiltonian of the Josephson junction, $\beta = 1/k_B T$, and U is an effective interaction strength. We neglect the U-dependent term which is independent of ϕ. One can further subtract a constant normal-state free energy $F(\Delta_s = 0)$ to avoid the divergence at large energies, and it would not affect the current-phase relation $I_s(\phi)$ [75]. The supercurrent through the JJ can be obtained from the free energy with

$$I_s(\phi) = \frac{2e}{\hbar}\frac{\partial F}{\partial \phi} = \frac{2e}{\hbar}\sum_{\epsilon_n} \frac{1}{e^{\beta\epsilon_n} + 1}\frac{\partial \epsilon_n}{\partial \phi}$$
$$= -\frac{2e}{\hbar}\sum_{\epsilon_n > 0} \tanh\left(\frac{\beta\epsilon_n}{2}\right)\frac{\partial \epsilon_n}{\partial \phi}. \qquad (B39)$$

Here, e is the charge of an electron. One can easily figure out the current units by using $\hbar \approx 6.581 \times 10^{-13}$ meV s and

$e/s \approx 1.6 \times 10^{-19}$ A (A denotes Ampere), i.e., $2e/\hbar \approx 486$ nA/meV.

By substituting the bound state energy Eq. (B30) into Eq. (B39), and at the high-temperature limit $\Delta_s/k_B T \ll 1$, we obtain Eq. (7) of the main text:

$$I_s(\phi) \approx \frac{e\Delta_s^2}{2\hbar k_B T}\cos\left(\frac{2\Delta_{vp}}{E_T}\right)\sin\left(\phi - \frac{\Delta_{vp}}{E_A}\right). \qquad (B40)$$

7. The scattering modes of different transverse momentum k_y

In the previous sections, we have solved the 1D scattering matrix problem for each mode at a fixed k_y. To obtain the total supercurrent through the junction, we need to insert different longitudinal Fermi momentum $v_{f,\tau\alpha}(k_y)$, and sum over different k_y that are quantized by the finite width. Unfortunately, we could not do it analytically due to the complicated warping effects. For completeness, we still present a brief discussion of the effects of k_y here.

The total supercurrent through this Josephson junction is given by

$$I_s(\phi) = \sum_{k_y} I_{s,k_y}(\phi). \qquad (B41)$$

In the short junction and at the high-temperature limit, the supercurrent at a phase difference ϕ, $I_{s,k_y}(\phi)$, carried by each mode can be obtained by replacing E_T, E_A in Eq. (B40) with the ones calculated from $v_{f,\tau\alpha}(k_y)$. As shown in Fig. 5(d), the value of longitudinal Fermi momentum $v_{f,\tau\alpha}(k_y)$ and its asymmetry near $k_y = 0$ are similar so that the resulting current-phase relation is expected to be similar to Eq. (B40) for a small transverse momentum. However, the situation becomes complicated in the large transverse momentum k_y. Because of the warping effects, there are multiple scattering modes near the Fermi energy for a fixed k_y [see Figs. 5(c) and 5(d)], which are not captured by Hamiltonian (B2), which only includes one incoming electron- or hole-dominant mode. Nevertheless, we expect the scattering modes with large momentum to carry less supercurrent, and thus in the main text we find that the 1D scattering Hamiltonian provides a good understanding of our numerical results, in which the current carried by all incoming modes is included.

APPENDIX C: MORE DETAILS FOR THE MATBG JOSEPHSON JUNCTION USING THE TIGHT-BINDING METHOD

In this Appendix, we present more details about the numerical calculations, including the geometry details, the result in the case of turning off the warping effects, and the result in the case of the weak-link region being a half-filling valley-polarized Chern insulator with a Chern number two.

1. Model and geometry details

As introduced in the main text, we adopt the following effective tight-binding model to capture the MATBG
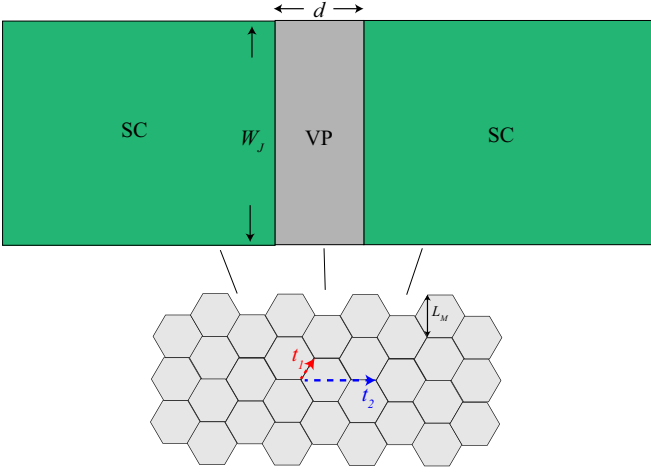
FIG. 7. The top panel presents the junction geometry that is adopted in the evaluation of Josephson supercurrent through the JJ using the effective tight-binding model H [Eq. (C1)]. d and W_J represent the junction length and width, respectively. Here SC and VP represent the regions with superconductivity and valley polarization. The bottom panel shows a hexagonal lattice used in the tight-binding model calculation, where t_1 denotes the first-nearest hopping, t_2 denotes the complex fifth-nearest hopping (resulting in warping term) in H, and the length of the next-nearest bond is L_M.

Josephson junction:

$$
\begin{aligned}
H_{\text{eff}} = & \sum_{\langle ij \rangle, \xi\sigma} t_1 c_{i\xi\sigma}^\dagger c_{j\xi\sigma} + \sum_{\langle ij \rangle', \xi\sigma} t_{2\xi\sigma} c_{i\xi\sigma}^\dagger c_{j\xi\sigma} + \text{H.c.} \\
& - \sum_{i,\xi} \mu_i c_{i\xi\sigma}^\dagger c_{i\xi\sigma} + \sum_{i\in(L,R),\xi} (\Delta_s e^{i\phi_{L(R)}} c_{i\xi\uparrow}^\dagger c_{i-\xi\downarrow}^\dagger \text{H.c.}) \\
& + \sum_{i\in WL, \xi\sigma} \Delta_{\text{vp}} c_{i\xi\sigma}^\dagger (\tau_z)_{\xi\xi'} c_{i\xi\sigma}.
\end{aligned} \tag{C1}
$$

See the main text for the detailed definitions of the ingredients in Hamiltonian H_{eff}. Here, we depict the adopted geometry of the MATBG Josephson junction in Fig. 7. The superconducting order parameter Δ_s and valley-polarized order parameter Δ_{vp} are added in the green region and the gray region of the top panel of Fig. 7, respectively. As shown in the bottom panel of Fig. 7, the lowest moiré bands near the charge neutrality are captured by hoppings on the two-orbital hexagonal lattice in each region, where t_1 represents the first-nearest hopping, and t_2 represents the complex fifth-nearest hopping (giving rise to the warping effects). We note that the minimal tight-binding model proposed in Ref. [4] that is used to capture the moiré bands up to the lowest hopping is narrower than that from the continuum model shown in Fig. 5(b). This, however, would not affect our result as the presence of φ_0-JJs is determined by the symmetries according to our main text analysis. The key length scales are also highlighted in Fig. 7. The lattice sites in Fig. 7 label the center of Wannier orbitals so that the length of the nearest bonds is the moiré lattice constant L_M. We thus measure the adopted junction length d and W in the main text in units of L_M.
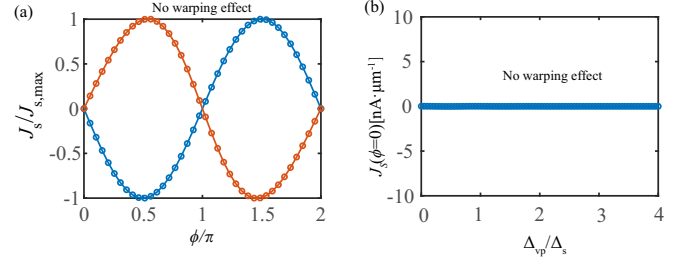

FIG. 8. The current-phase relation and vanishing of anomalous Josephson current in the case without warping effects. (a) Typical curves of Josephson current (normalized by its maximal value) vs Josephson phase difference ϕ of the MATBG Josephson junction when the warping term is turned off ($t_{2\xi} = 0$), which can only display 0- or π-junction behavior. (b) The anomalous Josephson current vanishes for various valley-polarization strengths where warping effects are not included.

2. Symmetry consideration

We now present a symmetry analysis to show why the valley polarization and the warping effects are crucial for the emergence of the φ_0-JJ in MATBG. Without these two ingredients, the system would exhibit time-reversal symmetry which gives $I_{s,\tau}(\phi) \mapsto -I_{s,-\tau}(-\phi)$, and an intravalley inversion symmetry which gives $I_{s,\tau}(\phi) \mapsto -I_{s,\tau}(-\phi)$. As $I_s(\phi) = \sum_\tau I_{s,\tau}(\phi)$, it can be seen that both symmetries would enforce the total supercurrent to satisfy the condition $I_s(\phi) = -I_s(-\phi)$, so that $I_s(\phi = 0) = 0$. Therefore, according to our symmetry analysis, the conclusion that the valley-polarized state induces φ_0-JJ is general as long as time-reversal and intravalley inversion symmetries are broken. Below, we present more cases to verify this symmetry analysis.

3. Case without warping effects

In the main text, the warping effects are naturally included in our calculations with the fifth-nearest hopping $t_{2\xi} \neq 0$ (cf. [4,5]). As discussed in the main text, the warping term would lift the intravalley inversion symmetry so that the minimal free energy of the junction is not necessarily 0- or π-JJ, resulting in a φ_0-JJ in general. To make a comparison, we now artificially turn off the warping term. As expected, we find that the junction is restricted to be 0- or π-JJ [Fig. 8(a)]. We consistently find that the anomalous Josephson current, i.e., $J_s(\phi = 0)$, vanishes [Fig. 8(b)]. It thus clearly shows that the warping effects are crucial for the ground state of MATBG Josephson junction to be φ_0-JJ, which is in agreement with our symmetry analysis presented in the main text.

4. Case with the junction region being valley-polarized Chern insulating states

It was pointed out in the main text that the valley-polarized state can mediate φ_0-JJs even when such state is topological nontrivial. In this section, as a demonstration, we present the calculated current-phase relation (Fig. 9) by setting the junction region to be half-filling ($\nu = -1/2$) valley-polarized Chern insulating states with Chern number $C = 2$ (see a
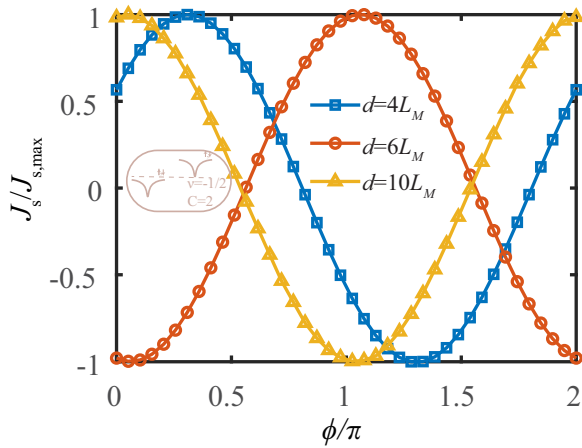
FIG. 9. The supercurrent density J_s (normalized by its maximal value) vs the phase difference ϕ with junction length $d = 4L_M, 6L_M, 10L_M$, where the junction region is set to be the valley-polarized Chern insulating states with $C = 2$ at half-filling that are illustrated with a schematic inset plot. Here we set the temperature $T = 0.05T_c$.

schematic illustration in the inset of Fig. 9). One can add a Haldane term to the tight-binding Hamiltonian (C1) in order to make the junction region topological (cf. Ref. [41]). In this case, as shown in Fig. 9, the curves of supercurrent J_s (normalized by its maximal value) versus the phase difference ϕ would still display a finite phase shift, i.e., $\sin(\phi - \varphi_0)$, for various junction lengths d. In other words, the junction would still behave as φ_0-JJ. Note that in the topological case, the edge states that can mediate some supercurrents may play an additional role. Nevertheless, Fig. 9 clearly shows that our conclusion about the valley polarization causing φ_0-JJ is not affected. It is understandable given that time-reversal and intravalley inversion symmetry are still broken by the valley-polarized Chern bands in this case.

APPENDIX D: THE MAGNETIC INTERFERENCE FOR φ_0-JOSEPHSON JUNCTIONS

1. Magnetic interference of a uniform φ_0-Josephson junction-standard Fraunhofer pattern

In this Appendix, we show that the magnetic interference of a uniform φ_0 Josephson junction should be the standard Fraunhofer pattern. The gauge-invariant phase difference across an extended junction is

$$\gamma = \tilde{\phi} + \frac{2e}{\hbar} \int \mathbf{A} \cdot d\mathbf{l} \tag{D1}$$

with $\tilde{\phi} = \phi - \varphi_0$, φ_0 denoting the phase shift in the φ_0-junction. For an out-of-plane magnetic field, the gauge can be chosen as $\mathbf{A} = (-By, 0)$. The Josephson current is given by

$$I_s = \int dy\, \boldsymbol{j}\left(\mathbf{r}, \tilde{\phi} - \frac{2e}{\hbar}\int_{-d/2}^{d/2} dx\, By\right). \tag{D2}$$

Assuming that the current follows the simplest $\sin(\phi - \varphi_0)$ feature, we will obtain

$$I_s = \int_{-W_J/2}^{W_J/2} dy\, j(y) \sin\left(\tilde{\phi} - \frac{2e}{\hbar} By d\right).$$

Here, we denote the width of the junction to be W_J. In the case of a uniform current density $j(x) = j_b$, then

$$I_s(\Phi) = \frac{j_b \sin\tilde{\phi} \sin(\pi\Phi/\Phi_0)}{\frac{\pi}{\Phi_0}BL}, \tag{D3}$$

where the flux quantum $\Phi_0 = h/2e$, $\Phi = B \times W_J d$. Thus,

$$I_c(\Phi) = I_c \left|\frac{\sin(\pi\Phi/\Phi_0)}{\pi\Phi/\Phi_0}\right|, \tag{D4}$$

where the critical current at zero-field is denoted as $I_c = j_0 W_J$. Hence, for a uniform φ_0 JJ, our phenomenological calculation suggests that the critical current as a function of external fields $I_c(\Phi)$ follows the standard Fraunhofer pattern.

2. Phenomenological theory for the magnetic interference of a φ_1-φ_2 Josephson junction

As we have mentioned in the main text, the total current through this junction under external magnetic fields can be written as

$$I_s(\phi) = \int_{-W_{J1}}^{0} dy\, j_b \sin\left(\phi - \varphi_1 - \frac{2e}{\hbar}By d\right)$$
$$+ \int_{0}^{W_{J2}} dy\, j_b \sin\left(\phi - \varphi_2 - \frac{2e}{\hbar}By d\right). \tag{D5}$$

Note that φ_1 and φ_2 would be different as Δ_{vp} in two domain walls are different. If $\varphi_1 = 0$ and $\varphi_2 = \pi$, the scenario would reduce to the 0-π JJ studied in Refs. [77–79], where the Fraunhofer pattern exhibits a dip near the zero magnetic flux due to the cancellation of the supercurrent of the 0-JJ parts and π-JJ parts. In our case, the φ_1 and φ_2 can be a value ranging from 0 to 2π due to the formation of φ_0-JJ. Hence, we call it φ_1-φ_2 JJ.

The Fraunhofer pattern of the φ_1-φ_2 JJ can be obtained from Eq. (D5). Specifically, the total supercurrent is written as

$$I_s(\phi) = \frac{I_{s1}}{2\pi\frac{\Phi_1}{\Phi_0}}\left[\cos(\phi - \varphi_1) - \cos\left(\phi - \varphi_1 + 2\pi\frac{\Phi_1}{\Phi_0}\right)\right]$$
$$+ \frac{I_{s2}}{2\pi\frac{\Phi_2}{\Phi_0}}\left[\cos\left(\phi - \varphi_2 - 2\pi\frac{\Phi_2}{\Phi_0}\right) - \cos(\phi - \varphi_2)\right]. \tag{D6}$$

Here, $I_{s1} = j_b W_{J1}$ and $I_{s2} = j_b W_{J2}$ denote the current through the two domain walls, respectively, and the magnetic flux though the jth domain wall is $\Phi_j = BW_j d$. For the sake of simplicity, we denote $I_{s1} = \frac{1}{2}(1 + \delta)I_s$, $I_{s2} = \frac{1}{2}(1 - \delta)I_s$, $\Phi_1 = \frac{1}{2}(1 + \delta)\Phi$, and $\Phi_2 = \frac{1}{2}(1 - \delta)\Phi$, where $I_s = I_{s1} + I_{s2}$ is the total supercurrent through the junction, and $\Phi = B(W_{J1} + W_{J2})d$ is the total magnetic flux. Using these

notations,

$$I_s(\phi) = \frac{I_s}{\frac{2\pi\Phi}{\Phi_0}}\left[\cos(\phi-\varphi_1) - \cos(\phi-\varphi_2) + \cos\left(\phi-\varphi_2\right.\right.$$
$$\left. - \frac{\pi(1-\delta)\Phi}{\Phi_0}\right) - \cos\left(\phi-\varphi_1 + \frac{\pi(1+\delta)\Phi}{\Phi_0}\right)\bigg]$$
$$= \frac{I_s}{\frac{\pi\Phi}{\Phi_0}}\left[\sin\left(\phi-\frac{\varphi_+}{2}+\delta\frac{\pi\Phi}{\Phi_0}\right)\sin\left(\frac{\varphi_-}{2}+\frac{\pi\Phi}{\Phi_0}\right)\right.$$
$$\left. - \sin\left(\phi-\frac{\varphi_+}{2}\right)\sin\left(\frac{\varphi_-}{2}\right)\right], \tag{D7}$$

where $\varphi_\pm = \varphi_2 \pm \varphi_1$.

The critical current $I_c = \max(I(\phi))$, given by the maximal value of $I_s(\phi)$ within $0 \leqslant \phi \leqslant 2\pi$. For the 0-0 JJ, one can easily obtain the standard Fraunhofer pattern $I_c(\Phi) = I_s\left|\frac{\sin(\pi\Phi/\Phi_0)}{\pi\Phi/\Phi_0}\right|$. Due to the presence of the asymmetry parameter δ, beyond 0-0 JJ, we could only find analytical solutions of the critical current in some special cases, such as in the limit of $\delta = 0$:

$$I_c(\Phi) = I_s\left|\frac{\sin\left(\frac{\varphi_-}{2}+\frac{\pi\Phi}{\Phi_0}\right) - \sin\left(\frac{\varphi_-}{2}\right)}{\frac{\pi\Phi}{\Phi_0}}\right|. \tag{D8}$$

It can be noted that the critical current is always zero if the magnetic flux reaches a certain integer flux quantum $\Phi = 2n\Phi_0$ (n are finite integers). As there is no node in the Fraunhofer pattern of experiments, we remove these nodes by introducing a finite asymmetric parameter δ. For example, at $\Phi = 2n\Phi_0$, the critical current becomes $I_s\left|\frac{\sin(\frac{\varphi_-}{2})\sin\delta n\pi}{2n\pi}\right|$, which could be finite if $\delta \neq 0$.

It is worth noting that another key feature of the experimentally observed Fraunhofer pattern is to exhibit $I_c(\Phi) \neq I_c(-\Phi)$. In the cases of 0-0 JJ and 0-π JJ, we find that the resulting Fraunhofer patterns are always symmetric, regardless of the choice of δ. However, if we consider φ_0-JJ, where $\varphi_\pm$ can take a more generic value rather than 0 or π, we find that the resulting Fraunhofer pattern is asymmetric in general. In Fig. 4 of the main text, we plotted the Fraunhofer pattern for the 0-0 JJ, 0-π JJ, and φ_1-φ_2 JJ with $\delta = 0.4$, $\varphi_1 = 0.2$, $\varphi_2 = \pi + 0.8$. The resulting Fraunhofer pattern arising from φ_1-φ_2 JJ is quite consistent with that seen in the experiment. Our calculation thus suggests that the presence of φ_0-JJs could provide a plausible explanation for such highly unconventional Fraunhofer patterns.

Here we further emphasize how the features of the unconventional pattern shown in the main text Fig. 4 are related to the φ_1-φ_2 JJ model, especially the model parameters φ_1, φ_2, δ: (i) The unconventional Fraunhofer pattern (red line), $|I_c(\Phi) \neq I_c(-\Phi)|$, which would indicate the time-reversal breaking. (ii) The unconventional Fraunhofer pattern exhibits a local minimal around zero flux. As a result, the central peak is shifted to a finite flux. It is sharply different from the conventional Fraunhofer pattern (gray line), which exhibits a maximal peak around zero flux. In the φ_1-φ_2 JJ, the local minimal appears around zero flux when the difference between φ_1 and φ_2 exceeds π, which results in a cancellation of supercurrent through φ_1 and φ_2 junction parts. (iii) The unconventional Fraunhofer pattern exhibits nonvanishing nodes at finite integer flux. According to the expression $I_c(\Phi = 2n\Phi_0)$,
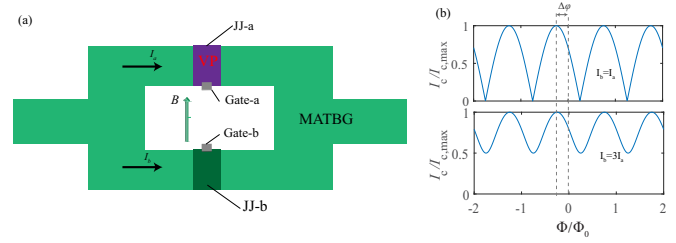

FIG. 10. (a) A schematic plot of a MATBG SQUID. Here, JJ-a represents a junction region controlled by gate-a, while JJ-b represents the other junction region controlled by gate-b. B is an out-of-plane magnetic field. (b) The critical supercurrent (normalized by its maximal value) as a function of the magnetic flux Φ in the case of $I_b = I_a$ (top panel) and $I_b = 3I_a$ (bottom panel). I_a and I_b are the supercurrent through JJ-a and JJ-b, respectively. The phase shift of the interference pattern $\Delta\varphi$ is highlighted.

the nonvanishing nodes at $\Phi = 2n\Phi_0$ indicate φ_1 and φ_2 are different, and W_{J1} and W_{J2} are different as $\delta \neq 0$.

3. Detection of φ_0-JJ with a superconducting MATBG SQUID

The SQUID can be used to identify the φ_0-JJ behavior in the experiments [67]. For the sake of completeness, as shown in Fig. 10(a), here we propose a MATBG SQUID geometry to detect the φ_0-JJ predicted by our theory. In this geometry, there are two weak-linked junction regions that are achieved by local gates a,b. Without loss of generality, we consider one is the $\varphi_0 - JJ$ with the junction gated into valley-polarized states (JJ-a), while the other one is the conventional JJ (JJ-b).

The total supercurrent through the SQUID under magnetic fields is written as

$$I_s = I_b \sin(\phi_b) + I_a \sin(\phi_a - \varphi_0) \tag{D9}$$

with

$$\varphi_b - \varphi_a = 2\pi\Phi/\Phi_0. \tag{D10}$$

Here, $I_a(\varphi_a)$ and $I_b(\varphi_b)$ are the supercurrent (phase difference) across the JJ-a and JJ-b, respectively. Φ is the magnetic flux through the SQUID. In a simple case where $I_a = I_b = I_0$, we can obtain the critical current at each magnetic flux as

$$I_c = 2I_0\left|\cos\left(\pi\frac{\Phi}{\Phi_0} + \frac{\varphi_0}{2}\right)\right|. \tag{D11}$$

Hence, the φ_0 would cause a phase shift in the SQUID pattern [see the top panel of Fig. 10(b)], where $\Delta\varphi = \varphi_0/2\pi$. In general, I_a and I_b are not equal. As an illustration, we plot the magnetic interference pattern with $I_b = 3I_a$ in Fig. 10(c). In this case, it can be seen that although the critical currents no longer vanish at certain magnetic fields, the phase shift does not change.

Therefore, the proposed MATBG SQUID provides a feasible way to directly measure the predicted φ_0 phase shift. Upon finishing our work, we noticed that the MATBG SQUID geometry has recently been successfully fabricated in the experiment [42]. Our work thus would motive experimentalists to further gate the junction region into valley-polarized states and study the proposed unconventional Josephson effects in the near future.

TABLE I. Classifications of all possible momentum-independent pairing of TBG according to the irreducible representations of the D_3 symmetry group.

IRs	A_1	A_2	E
$C_{3z} = \tau_0 \otimes e^{-i\frac{\pi}{3}\sigma_z}$	$+1$	$+1$	$+2$
$C_{2y} = \tau_x \otimes i\sigma_y$	$+1$	$+1$	0
Spin-singlet	$\tau_x \otimes i\sigma_y$		
Spin-triplet	$i\tau_y \otimes \sigma_x$		$(i\tau_y \otimes \sigma_z, i\tau_y \otimes \sigma_0)$

APPENDIX E: THE φ_0-JJ BEYOND CONVENTIONAL PAIRINGS

In the main text, to be specific, we have adopted the spin-singlet pairing as the pairing order parameter for the superconducting part of the MATBG Josephson junction. In this Appendix, we point out that the φ_0-JJ can still persist even when the pairing is unconventional, such as various spin-triplet pairings. The pairings can be expanded in the space formed by spin and valley degrees of freedom. We first classify the possible pairings using irreducible representations of the D_3 crystal group of MATBG. For simplicity, we focus on all **k**-independent intervalley pairings.

Specifically, the generators of D_3 point contain a threefold rotation along the z-axis represented by $C_{3z} = \tau_0 \otimes e^{-i\frac{\pi}{3}\sigma_z}$, and a twofold rotation along the y-axis represented by $C_{2y} = \tau_x \otimes i\sigma_y$. Here, σ and τ are Pauli matrices defined in spin- and valley-space. Note that C_{2y} would exchange the K and $-K$ valley, while C_3 would not.

The pairing matrix transforms under the point group symmetry operation as

$$g\hat{\Delta}_s \mapsto U^\dagger(g)\hat{\Delta}_s U^*(g), \quad \text{(E1)}$$

where $\hat{\Delta}_s$ is defined in the Nambu basis: $(\psi_{+,\uparrow}, \psi_{+,\downarrow}, \psi_{-,\uparrow}, \psi_{-,\downarrow})^T$ with $+/-$ as valley index and $\uparrow / \downarrow$ for spin-up/spin-down, and $U(g)$ is the matrix representation of the generator g in the spin and valley space. Note that $\hat{\Delta}_s = -\hat{\Delta}_s^T$ due to the Fermi statistics, and the representation of $\hat{\Delta}_s$ in the valley degree of freedom is restricted to be τ_x and τ_y, i.e., intervalley nature. All the **k**-independent intervalley pairings are summarized in Table I.

There is one intervalley spin-singlet A_1 pairing : $\Delta_{A_1,s} = \tau_x \otimes i\sigma_y$, and there are two inter-valley spin-triplet pairings: one one-dimensional spin-triplet A_1-pairing $\Delta_{A_1,t} = i\tau_y \otimes \sigma_x$, and one two-dimensional spin-triplet E-pairing, which we label as E_1-pairing and E_2-pairing with $(\Delta_{E,1}, \Delta_{E,2}) = (i\tau_y \otimes \sigma_z, i\tau_y \otimes \sigma_0)$. Note that the pairings labeled by different irreducible representations do not mix, and the mixing of $\Delta_{A_1,s}$ and $\Delta_{A_1,t}$ is expected to be neglectable as the spin-orbit coupling in graphene is extremely small. It is also worth noting that the possible nematic pairings can be constructed using the pairing matrices in two-dimensional E-pairing.

We can replace the order parameter of the superconducting part with the above unconventional momentum-independent pairings in the previous tight-binding model calculation and evaluate the supercurrent in the same way. As shown in Figs. 11(a)–11(d), we find that the current-phase relation is unchanged in the cases of various spin-triplet pairings, which thus implies that our result is not sensitive to the spin
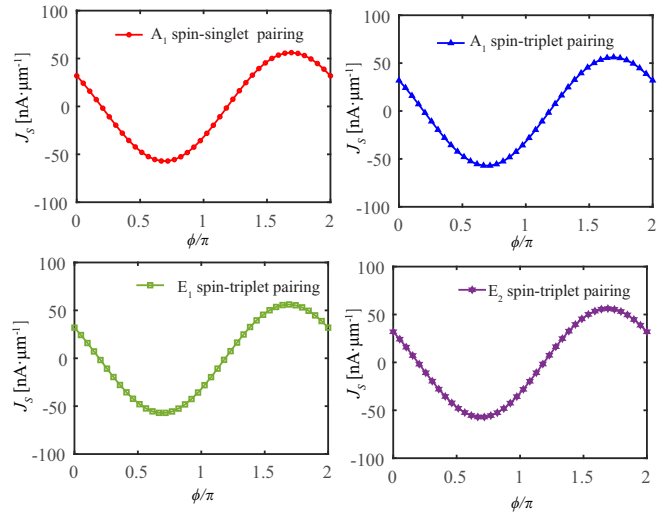

FIG. 11. (a)–(d) The supercurrent density J_s (in units of nA μm^{-1}) vs the Josephson phase difference ϕ for A_1 spin-singlet pairing, A_1 spin-triplet pairings, E_1 spin-triplet pairing, and E_2 spin-triplet pairing, respectively. Here we adopt a valley-polarization strength $\Delta_{vp}/\Delta_s = 3$ and a temperature $T/T_c = 0.3$.

configurations of Cooper pairs of the superconducting part. This observation is understandable as the appearance of φ_0-JJ is mainly induced by the valley polarization of the junction region.

APPENDIX F: A COMPARISON BETWEEN OUR MODEL AND THE φ_0 JJ MODEL ARISING FROM EXCHANGE FIELDS AND SPIN-ORBIT COUPLING

In the main text, we pointed out that the warping term and valley-polarization effectively, respectively, play the role of exchange fields and spin-orbit coupling in comparison with previous φ_0 JJ models with these terms. Here we illustrate this with more detail. To map the trigonal warping term as a spin-orbit coupling, we can look at the $k \cdot p$ normal state Hamiltonian of our system before linearization as shown in Sec. I:

$$H_N = \lambda_0\big(k_x^2 + k_y^2\big) + \lambda_1\big[k_x\big(k_x^2 - 3k_y^2\big) + \Delta_{vp}\big]\tau_z. \quad \text{(F1)}$$

Note that the normal part of the phenomenological model in the main text [Eq. (3)] is given by linearizing the momentum near Fermi energy.

If we regard the valley as a pseudospin, the trigonal warping term $\lambda_1 k_x(k_x^2 - 3k_y^2)\tau_z$ indeed can be regarded as a spin-orbit coupling, and $\Delta_{vp}\tau_z$ can be regarded as a polarization induced by an exchange field. When we consider the Josephson junction, k_y can be fixed as a good number by setting the current direction to be the k_x-direction. For simplicity, we set $k_y = 0$ as we considered the phenomenological model Eq. (3), and then $H_{N,1D} = \lambda_0 k_x^2 + [\lambda_1 k_x^3 + \Delta_{vp}]\tau_z$.

Next, we highlight the similarities between our model and the Rashba nanowire model, which can be written as $H_R = k_x^2/2m + \alpha k_x \sigma_y + h\sigma_y$, with the $h\sigma_y$ denoting the Zeeman coupling of the magnetic field with the spin of the electron in the y-direction, and α is the strength of the Rashba spin-orbit

coupling. It is known that the Rashba spin-orbit coupling combined with an in-plane spin polarization would result in the φ_0 JJ. Our $H_{N,1D}$ model (with $k_y = 0$) is equivalent to replacing the Rashba spin-orbit coupling model with a cubic warping term, which can be seen by performing a unitary transformation mapping τ_z to τ_y in $H_{N,1D}$: $H'_{N,1D} = \lambda_0 k_x^2 + \lambda_1 (k_x^3 + \Delta_{vp}) \tau_y$. After this mapping, it is indeed understandable that we can get a φ_0 JJ.

However, it should be noted that the underlying physical system in our case is very different, given that the polarization appears in valley degrees of freedom rather than spin. Our proposal relies on the valley-polarized moiré bands, and it does not need to involve spin-orbit coupling or exchange fields. Only when we restrict the game interaction-induced order

parameter to the valley polarization $\Delta_{vp} \tau_z$ can our model be mapped to the model with Rashba SOC in some limit. Indeed, the interaction-induced order parameter can be richer. Another difference we would like to highlight here is that the possessing of both spin and valley degrees of freedom in moiré bands allows much more rich cases with various band alignment. For example, the spin–valley-polarized state can also appear at very low temperatures in the experiment [41]. In this case, the order parameter can be written as $\Delta_{vp} \tau_z \sigma_0 + \Delta_{sp} \tau_0 \otimes \sigma_z$. Both the spin polarization and the valley polarization would contribute to the anomalous phase shift. However, this model cannot be generally mapped to a Rashba spin-orbit coupling model as we would deal with a 4 by 4 matrix with two kinds of polarization.

[1] R. Bistritzer and A. H. MacDonald, Moiré bands in twisted double-layer graphene, Proc. Natl. Acad. Sci. USA **108**, 12233 (2011).

[2] Y. Cao, V. Fatemi, A. Demir, S. Fang, S. L. Tomarken, J. Y. Luo, J. D. Sanchez-Yamagishi, K. Watanabe, T. Taniguchi, E. Kaxiras, R. C. Ashoori, and P. Jarillo-Herrero, Correlated insulator behaviour at half-filling in magic-angle graphene superlattices, Nature (London) **556**, 80 (2018).

[3] Y. Cao, V. Fatemi, S. Fang, K. Watanabe, T. Taniguchi, E. Kaxiras, and P. Jarillo-Herrero, Unconventional superconductivity in magic-angle graphene superlattices, Nature (London) **556**, 43 (2018).

[4] M. Koshino, N. F. Q. Yuan, T. Koretsune, M. Ochi, K. Kuroki, and L. Fu, Maximally Localized Wannier Orbitals and the Extended Hubbard Model for Twisted Bilayer Graphene, Phys. Rev. X **8**, 031087 (2018).

[5] N. F. Q. Yuan and L. Fu, Model for the metal-insulator transition in graphene superlattices and beyond, Phys. Rev. B **98**, 045103 (2018).

[6] H. Isobe, N. F. Q. Yuan, and L. Fu, Unconventional Superconductivity and Density Waves in Twisted Bilayer Graphene, Phys. Rev. X **8**, 041041 (2018).

[7] C.-C. Liu, L.-D. Zhang, W.-Q. Chen, and F. Yang, Chiral Spin Density Wave and $d + id$ Superconductivity in the Magic-Angle-Twisted Bilayer Graphene, Phys. Rev. Lett. **121**, 217001 (2018).

[8] F. Wu, A. H. MacDonald, and I. Martin, Theory of Phonon-Mediated Superconductivity in Twisted Bilayer Graphene, Phys. Rev. Lett. **121**, 257001 (2018).

[9] C. Xu and L. Balents, Topological Superconductivity in Twisted Multilayer Graphene, Phys. Rev. Lett. **121**, 087001 (2018).

[10] B. Lian, Z. Wang, and B. A. Bernevig, Twisted Bilayer Graphene: A Phonon-Driven Superconductor, Phys. Rev. Lett. **122**, 257002 (2019).

[11] Y. Jiang, X. Lai, K. Watanabe, T. Taniguchi, K. Haule, J. Mao, and E. Y. Andrei, Charge order and broken rotational symmetry in magic-angle twisted bilayer graphene, Nature (London) **573**, 91 (2019).

[12] J. González and T. Stauber, Kohn-Luttinger Superconductivity in Twisted Bilayer Graphene, Phys. Rev. Lett. **122**, 026801 (2019).

[13] M. Yankowitz, S. Chen, H. Polshyn, Y. Zhang, K. Watanabe, T. Taniguchi, D. Graf, A. F. Young, and C. R. Dean, Tuning

superconductivity in twisted bilayer graphene, Science **363**, 1059 (2019).

[14] A. Kerelsky, L. J. McGilly, D. M. Kennes, L. Xian, M. Yankowitz, S. Chen, K. Watanabe, T. Taniguchi, J. Hone, C. Dean, A. Rubio, and A. N. Pasupathy, Maximized electron interactions at the magic angle in twisted bilayer graphene, Nature (London) **572**, 95 (2019).

[15] Y. Xie, B. Lian, B. Jäck, X. Liu, C.-L. Chiu, K. Watanabe, T. Taniguchi, B. A. Bernevig, and A. Yazdani, Spectroscopic signatures of many-body correlations in magic-angle twisted bilayer graphene, Nature (London) **572**, 101 (2019).

[16] Y. Choi, J. Kemmer, Y. Peng, A. Thomson, H. Arora, R. Polski, Y. Zhang, H. Ren, J. Alicea, G. Refael, F. von Oppen, K. Watanabe, T. Taniguchi, and S. Nadj-Perge, Electronic correlations in twisted bilayer graphene near the magic angle, Nat. Phys. **15**, 1174 (2019).

[17] X. Lu, P. Stepanov, W. Yang, M. Xie, M. A. Aamir, I. Das, C. Urgell, K. Watanabe, T. Taniguchi, G. Zhang, A. Bachtold, A. H. MacDonald, and D. K. Efetov, Superconductors, orbital magnets and correlated states in magic-angle bilayer graphene, Nature (London) **574**, 653 (2019).

[18] A. L. Sharpe, E. J. Fox, A. W. Barnard, J. Finney, K. Watanabe, T. Taniguchi, M. A. Kastner, and D. Goldhaber-Gordon, Emergent ferromagnetism near three-quarters filling in twisted bilayer graphene, Science **365**, 605 (2019).

[19] M. Serlin, C. L. Tschirhart, H. Polshyn, Y. Zhang, J. Zhu, K. Watanabe, T. Taniguchi, L. Balents, and A. F. Young, Intrinsic quantized anomalous Hall effect in a moiré heterostructure, Science **367**, 900 (2020).

[20] P. Stepanov, I. Das, X. Lu, A. Fahimniya, K. Watanabe, T. Taniguchi, F. H. L. Koppens, J. Lischner, L. Levitov, and D. K. Efetov, Untying the insulating and superconducting orders in magic-angle graphene, Nature (London) **583**, 375 (2020).

[21] D. Wong, K. P. Nuckolls, M. Oh, B. Lian, Y. Xie, S. Jeon, K. Watanabe, T. Taniguchi, B. A. Bernevig, and A. Yazdani, Cascade of electronic transitions in magic-angle twisted bilayer graphene, Nature (London) **582**, 198 (2020).

[22] J. Kang and O. Vafek, Strong Coupling Phases of Partially Filled Twisted Bilayer Graphene Narrow Bands, Phys. Rev. Lett. **122**, 246401 (2019).

[23] Z. Song, Z. Wang, W. Shi, G. Li, C. Fang, and B. A. Bernevig, All Magic Angles in Twisted Bilayer Graphene are Topological, Phys. Rev. Lett. **123**, 036401 (2019).

[24] Y. Saito, J. Ge, K. Watanabe, T. Taniguchi, and A. F. Young, Independent superconductors and correlated insulators in twisted bilayer graphene, Nat. Phys. **16**, 926 (2020).

[25] U. Zondiner, A. Rozen, D. Rodan-Legrain, Y. Cao, R. Queiroz, T. Taniguchi, K. Watanabe, Y. Oreg, F. von Oppen, A. Stern, E. Berg, P. Jarillo-Herrero, and S. Ilani, Cascade of phase transitions and Dirac revivals in magic-angle graphene, Nature (London) **582**, 203 (2020).

[26] Y. Choi, H. Kim, Y. Peng, A. Thomson, C. Lewandowski, R. Polski, Y. Zhang, H. S. Arora, K. Watanabe, T. Taniguchi, J. Alicea, and S. Nadj-Perge, Correlation-driven topological phases in magic-angle twisted bilayer graphene, Nature (London) **589**, 536 (2021).

[27] Y.-T. Hsu, F. Wu, and S. Das Sarma, Topological superconductivity, ferromagnetism, and valley-polarized phases in moiré systems: Renormalization group analysis for twisted double bilayer graphene, Phys. Rev. B **102**, 085103 (2020).

[28] H. C. Po, L. Zou, A. Vishwanath, and T. Senthil, Origin of Mott Insulating Behavior and Superconductivity in Twisted Bilayer Graphene, Phys. Rev. X **8**, 031089 (2018).

[29] Y.-H. Zhang, D. Mao, Y. Cao, P. Jarillo-Herrero, and T. Senthil, Nearly flat chern bands in moiré superlattices, Phys. Rev. B **99**, 075127 (2019).

[30] M. Xie and A. H. MacDonald, Nature of the Correlated Insulator States in Twisted Bilayer Graphene, Phys. Rev. Lett. **124**, 097601 (2020).

[31] N. Bultinck, S. Chatterjee, and M. P. Zaletel, Mechanism for Anomalous Hall Ferromagnetism in Twisted Bilayer Graphene, Phys. Rev. Lett. **124**, 166601 (2020).

[32] N. Bultinck, E. Khalaf, S. Liu, S. Chatterjee, A. Vishwanath, and M. P. Zaletel, Ground State and Hidden Symmetry of Magic-Angle Graphene at Even Integer Filling, Phys. Rev. X **10**, 031034 (2020).

[33] T. Cea and F. Guinea, Band structure and insulating states driven by Coulomb interaction in twisted bilayer graphene, Phys. Rev. B **102**, 045107 (2020).

[34] Y. Zhang, K. Jiang, Z. Wang, and F. Zhang, Correlated insulating phases of twisted bilayer graphene at commensurate filling fractions: A Hartree-Fock study, Phys. Rev. B **102**, 035136 (2020).

[35] J. Liu and X. Dai, Theories for the correlated insulating states and quantum anomalous Hall effect phenomena in twisted bilayer graphene, Phys. Rev. B **103**, 035427 (2021).

[36] G. Shavit, E. Berg, A. Stern, and Y. Oreg, Theory of Correlated Insulators and Superconductivity in Twisted Bilayer Graphene, Phys. Rev. Lett. **127**, 247703 (2021).

[37] Y. Cao, D. Rodan-Legrain, J. M. Park, N. F. Q. Yuan, K. Watanabe, T. Taniguchi, R. M. Fernandes, L. Fu, and P. Jarillo-Herrero, Nematicity and competing orders in superconducting magic-angle graphene, Science **372**, 264 (2021).

[38] A. O. Sboychakov, A. V. Rozhkov, A. L. Rakhmanov, and F. Nori, Spin density wave and electron nematicity in magic-angle twisted bilayer graphene, Phys. Rev. B **102**, 155142 (2020).

[39] D. Rodan-Legrain, Y. Cao, J. M. Park, S. C. de la Barrera, M. T. Randeria, K. Watanabe, T. Taniguchi, and P. Jarillo-Herrero, Highly tunable junctions and non-local Josephson effect in magic-angle graphene tunnelling devices, Nat. Nanotechnol. **16**, 769 (2021).

[40] F. K. de Vries, E. Portolés, G. Zheng, T. Taniguchi, K. Watanabe, T. Ihn, K. Ensslin, and P. Rickhaus, Gate-defined Josephson junctions in magic-angle twisted bilayer graphene, Nat. Nanotechnol. **16**, 760 (2021).

[41] J. Diez-Merida, A. Diez-Carlon, S. Y. Yang, Y.-M. Xie, X.-J. Gao, K. Watanabe, T. Taniguchi, X. Lu, K. T. Law, and D. K. Efetov, Magnetic Josephson junctions and superconducting diodes in magic angle twisted bilayer graphene arXiv:2110.01067 (2021).

[42] E. Portolés, S. Iwakiri, G. Zheng, P. Rickhaus, T. Taniguchi, K. Watanabe, T. Ihn, K. Ensslin, and F. K. de Vries, A tunable monolithic squid in twisted bilayer graphene, Nat. Nanotechnol. **17**, 1159 (2022).

[43] C.-C. Tseng, X. Ma, Z. Liu, K. Watanabe, T. Taniguchi, J.-H. Chu, and M. Yankowitz, Anomalous Hall effect at half filling in twisted bilayer graphene, Nat. Phys. **18**, 1038 (2022).

[44] J. Linder and J. W. A. Robinson, Superconducting spintronics, Nat. Phys. **11**, 307 (2015).

[45] M. Eschrig, Spin-polarized supercurrents for spintronics: A review of current progress, Rep. Prog. Phys. **78**, 104501 (2015).

[46] L. B. Ioffe, V. B. Geshkenbein, M. V. Feigel'man, A. L. Fauchère, and G. Blatter, Environmentally decoupled SDS-wave Josephson junctions for quantum computing, Nature (London) **398**, 679 (1999).

[47] T. Yamashita, K. Tanikawa, S. Takahashi, and S. Maekawa, Superconducting π Qubit with a Ferromagnetic Josephson Junction, Phys. Rev. Lett. **95**, 097001 (2005).

[48] C. Padurariu and Y. V. Nazarov, Theoretical proposal for superconducting spin qubits, Phys. Rev. B **81**, 144519 (2010).

[49] E. Strambini, A. Iorio, O. Durante, R. Citro, C. Sanz-Fernández, C. Guarcello, I. V. Tokatly, A. Braggio, M. Rocci, N. Ligato, V. Zannier, L. Sorba, F. S. Bergeret, and F. Giazotto, A Josephson phase battery, Nat. Nanotechnol. **15**, 656 (2020).

[50] V. Braude and Y. V. Nazarov, Fully Developed Triplet Proximity Effect, Phys. Rev. Lett. **98**, 077003 (2007).

[51] R. Grein, M. Eschrig, G. Metalidis, and G. Schön, Spin-Dependent Cooper Pair Phase and Pure Spin Supercurrents in Strongly Polarized Ferromagnets, Phys. Rev. Lett. **102**, 227005 (2009).

[52] B. Béri, J. N. Kupferschmidt, C. W. J. Beenakker, and P. W. Brouwer, Quantum limit of the triplet proximity effect in half-metal–superconductor junctions, Phys. Rev. B **79**, 024517 (2009).

[53] H. Enoksen, J. Linder, and A. Sudbø, Spin-flip scattering and critical currents in ballistic half-metallic d-wave Josephson junctions, Phys. Rev. B **85**, 014512 (2012).

[54] F. Konschelle and A. Buzdin, Magnetic Moment Manipulation by a Josephson Current, Phys. Rev. Lett. **102**, 017001 (2009).

[55] J.-F. Liu and K. S. Chan, Anomalous Josephson current through a ferromagnetic trilayer junction, Phys. Rev. B **82**, 184533 (2010).

[56] M. A. Silaev, I. V. Tokatly, and F. S. Bergeret, Anomalous current in diffusive ferromagnetic Josephson junctions, Phys. Rev. B **95**, 184508 (2017).

[57] A. Buzdin, Direct Coupling Between Magnetism and Superconducting Current in the Josephson φ_0 Junction, Phys. Rev. Lett. **101**, 107005 (2008).

[58] S. Mironov and A. Buzdin, Spontaneous Currents in Superconducting Systems with Strong Spin-Orbit Coupling, Phys. Rev. Lett. **118**, 077001 (2017).

[59] A. A. Reynoso, G. Usaj, C. A. Balseiro, D. Feinberg, and M. Avignon, Anomalous Josephson Current in Junctions with

Spin Polarizing Quantum Point Contacts, Phys. Rev. Lett. **101**, 107001 (2008).

[60] A. Zazunov, R. Egger, T. Jonckheere, and T. Martin, Anomalous Josephson Current through a Spin-Orbit Coupled Quantum Dot, Phys. Rev. Lett. **103**, 147004 (2009).

[61] T. Yokoyama, M. Eto, and Y. V. Nazarov, Anomalous Josephson effect induced by spin-orbit interaction and Zeeman effect in semiconductor nanowires, Phys. Rev. B **89**, 195407 (2014).

[62] Y. Tanaka, T. Yokoyama, and N. Nagaosa, Manipulation of the Majorana Fermion, Andreev Reflection, and Josephson Current on Topological Insulators, Phys. Rev. Lett. **103**, 107002 (2009).

[63] F. Dolcini, M. Houzet, and J. S. Meyer, Topological Josephson ϕ_0 junctions, Phys. Rev. B **92**, 035428 (2015).

[64] F. S. Bergeret and I. V. Tokatly, Theory of diffusive ϕ_0 Josephson junctions in the presence of spin-orbit coupling, Europhys. Lett. **110**, 57005 (2015).

[65] F. Konschelle, I. V. Tokatly, and F. S. Bergeret, Theory of the spin-galvanic effect and the anomalous phase shift φ_0 in superconductors and Josephson junctions with intrinsic spin-orbit coupling, Phys. Rev. B **92**, 125443 (2015).

[66] K. Sakurai, S. Ikegaya, and Y. Asano, Tunable-φ Josephson junction with a quantum anomalous Hall insulator, Phys. Rev. B **96**, 224514 (2017).

[67] D. B. Szombati, S. Nadj-Perge, D. Car, S. R. Plissard, E. P. A. M. Bakkers, and L. P. Kouwenhoven, Josephson φ_0-junction in nanowire quantum dots, Nat. Phys. **12**, 568 (2016).

[68] A. Assouline, C. Feuillet-Palma, N. Bergeal, T. Zhang, A. Mottaghizadeh, A. Zimmers, E. Lhuillier, M. Eddrie, P. Atkinson, M. Aprili, and H. Aubin, Spin-Orbit induced phase-shift in Bi_2Se_3 Josephson junctions, Nat. Commun. **10**, 126 (2019).

[69] W. Mayer, M. C. Dartiailh, J. Yuan, K. S. Wickramasinghe, E. Rossi, and J. Shabani, Gate controlled anomalous phase shift in Al/InAs Josephson junctions, Nat. Commun. **11**, 212 (2020).

[70] M. Alidoust, C. Shen, and I. Žutić, Cubic spin-orbit coupling and anomalous Josephson effect in planar junctions, Phys. Rev. B **103**, L060503 (2021).

[71] F. Wu and S. Das Sarma, Collective Excitations of Quantum Anomalous Hall Ferromagnets in Twisted Bilayer Graphene, Phys. Rev. Lett. **124**, 046403 (2020).

[72] M. Oh, K. P. Nuckolls, D. Wong, R. L. Lee, X. Liu, K. Watanabe, T. Taniguchi, and A. Yazdani, Evidence for unconventional superconductivity in twisted bilayer graphene, Nature (London) **600**, 240 (2021).

[73] M. Tinkham, *Introduction to Superconductivity* (Dover Publications, Mineola, NY, 2004).

[74] C. W. J. Beenakker, Universal Limit of Critical-Current Fluctuations in Mesoscopic Josephson Junctions, Phys. Rev. Lett. **67**, 3836 (1991).

[75] C. W. J. Beenakker, Three universal mesoscopic Josephson effects, in *Transport Phenomena in Mesoscopic Systems*, edited by H. Fukuyama and T. Ando (Springer, 1992), pp. 235–253.

[76] S. Grover, M. Bocarsly, A. Uri, P. Stepanov, G. Di Battista, I. Roy, J. Xiao, A. Y. Meltzer, Y. Myasoedov, K. Pareek, K. Watanabe, T. Taniguchi, B. Yan, A. Stern, E. Berg, D. K. Efetov, and E. Zeldov, Chern mosaic and Berry-curvature magnetism in magic-angle graphene, Nat. Phys. **18**, 885 (2022).

[77] M. Weides, M. Kemmler, H. Kohlstedt, R. Waser, D. Koelle, R. Kleiner, and E. Goldobin, $0-\pi$ Josephson tunnel junctions with ferromagnetic barrier, Phys. Rev. Lett. **97**, 247001 (2006).

[78] S. M. Frolov, D. J. Van Harlingen, V. V. Bolginov, V. A. Oboznov, and V. V. Ryazanov, Josephson interferometry and Shapiro step measurements of superconductor-ferromagnet-superconductor $0-\pi$ junctions, Phys. Rev. B **74**, 020503(R) (2006).

[79] M. Kemmler, M. Weides, M. Weiler, M. Opel, S. T. B. Goennenwein, A. S. Vasenko, A. A. Golubov, H. Kohlstedt, D. Koelle, R. Kleiner, and E. Goldobin, Magnetic interference patterns in $0-\pi$ superconductor/insulator/ferromagnet/superconductor Josephson junctions: Effects of asymmetry between 0 and π regions, Phys. Rev. B **81**, 054522 (2010).

[80] Y. Lu and T. T. Heikkilä, Proximity effect in superconducting heterostructures with strong spin-orbit coupling and spin splitting, Phys. Rev. B **100**, 104514 (2019).